This paper is published as part of a PCCP Themed Issue on:

Modern EPR Spectroscopy: Beyond the EPR Spectrum

Guest Editor: Daniella Goldfarb

Editorial

Perspective

Communication

Papers

A W-band pulsed EPR/ENDOR study of $Co^{II}S_4$ coordination in the $Co[(SPPh_2)(SP^iPr_2)N]_2$ complex
Silvia Sottini, Guinevere Mathies, Peter Gast, Dimitrios Maganas, Panayotis Kyritsis and Edgar J.J. Groenen, *Phys. Chem. Chem. Phys.*, 2009
DOI: 10.1039/b905726a

Exchangeable oxygens in the vicinity of the molybdenum center of the high-pH form of sulfite oxidase and sulfite dehydrogenase
Andrei V. Astashkin, Eric L. Klein, Dmitry Ganyushin, Kayunta Johnson-Winters, Frank Neese, Ulrike Kappler and John H. Enemark, *Phys. Chem. Chem. Phys.*, 2009
DOI: 10.1039/b907029j

Magnetic quantum tunneling: key insights from multi-dimensional high-field EPR
J. Lawrence, E.-C. Yang, D. N. Hendrickson and S. Hill, *Phys. Chem. Chem. Phys.*, 2009
DOI: 10.1039/b908460f

Spin-dynamics of the spin-correlated radical pair in photosystem I. Pulsed time-resolved EPR at high magnetic field
O. G. Poluektov, S. V. Paschenko and L. M. Utschig, *Phys. Chem. Chem. Phys.*, 2009
DOI: 10.1039/b906521k

Enantioselective binding of structural epoxide isomers by a chiral vanadyl salen complex: a pulsed EPR, cw-ENDOR and DFT investigation
Damien M. Murphy, Ian A. Fallis, Emma Carter, David J. Willock, James Landon, Sabine Van Doorslaer and Evi Vinck, *Phys. Chem. Chem. Phys.*, 2009
DOI: 10.1039/b907807j

Topology of the amphipathic helices of the colicin A pore-forming domain in *E. coli* lipid membranes studied by pulse EPR
Sabine Böhme, Pulagam V. L. Padmavathi, Julia Holterhues, Fatiha Ouchni, Johann P. Klare and Heinz-Jürgen Steinhoff, *Phys. Chem. Chem. Phys.*, 2009
DOI: 10.1039/b907117m

Structural characterization of a highly active superoxide-dismutase mimic
Vimalkumar Balasubramanian, Maria Ezhevskaya, Hans Moons, Markus Neuburger, Carol Cristescu, Sabine Van Doorslaer and Cornelia Palivan, *Phys. Chem. Chem. Phys.*, 2009
DOI: 10.1039/b905593b

Structure of the oxygen-evolving complex of photosystem II: information on the S_2 state through quantum chemical calculation of its magnetic properties
Dimitrios A. Pantazis, Maylis Orio, Taras Petrenko, Samir Zein, Wolfgang Lubitz, Johannes Messinger and Frank Neese, *Phys. Chem. Chem. Phys.*, 2009
DOI: 10.1039/b907038a

Population transfer for signal enhancement in pulsed EPR experiments on half integer high spin systems
Ilia Kaminker, Alexey Potapov, Akiva Feintuch, Shimon Vega and Daniella Goldfarb, *Phys. Chem. Chem. Phys.*, 2009
DOI: 10.1039/b906177k

The reduced [2Fe-2S] clusters in adrenodoxin and *Arthrospira platensis* ferredoxin share spin density with protein nitrogens, probed using 2D ESEEM
Sergei A. Dikanov, Rimma I. Samoilova, Reinhard Kappl, Antony R. Crofts and Jürgen Hüttermann, *Phys. Chem. Chem. Phys.*, 2009
DOI: 10.1039/b904597j

Frequency domain Fourier transform THz-EPR on single molecule magnets using coherent synchrotron radiation
Alexander Schnegg, Jan Behrends, Klaus Lips, Robert Bittl and Karsten Holldack, *Phys. Chem. Chem. Phys.*, 2009
DOI: 10.1039/b905745e

PELDOR study of conformations of double-spin-labeled single- and double-stranded DNA with non-nucleotide inserts
Nikita A. Kuznetsov, Alexandr D. Milov, Vladimir V. Koval, Rimma I. Samoilova, Yuri A. Grishin, Dmitry G. Knorre, Yuri D. Tsvetkov, Olga S. Fedorova and Sergei A. Dzuba, *Phys. Chem. Chem. Phys.*, 2009
DOI: 10.1039/b904873a

Site-specific dynamic nuclear polarization of hydration water as a generally applicable approach to monitor protein aggregation
Anna Pavlova, Evan R. McCarney, Dylan W. Peterson, Frederick W. Dahlquist, John Lew and Songi Han, *Phys. Chem. Chem. Phys.*, 2009
DOI: 10.1039/b906101k

Structural information from orientationally selective DEER spectroscopy
J. E. Lovett, A. M. Bowen, C. R. Timmel, M. W. Jones, J. R. Dilworth, D. Caprotti, S. G. Bell, L. L. Wong and J. Harmer, *Phys. Chem. Chem. Phys.*, 2009
DOI: 10.1039/b907010a

Structure and bonding of $[V^{IV}O(acac)_2]$ on the surface of AlF_3 as studied by pulsed electron nuclear double resonance and hyperfine sublevel correlation spectroscopy
Vijayasarathi Nagarajan, Barbara Müller, Oksana Storcheva, Klaus Köhler and Andreas Pöppl, *Phys. Chem. Chem. Phys.*, 2009
DOI: 10.1039/b903826b

Local variations in defect polarization and covalent bonding in ferroelectric Cu2+-doped PZT and KNN functional ceramics at themorphotropic phase boundary
Rüdiger-A. Eichel, Ebru Erünal, Michael D. Drahus, Donald M. Smyth, Johan van Tol, Jérôme Acker, Hans Kungl and Michael J. Hoffmann, *Phys. Chem. Chem. Phys.*, 2009
DOI: 10.1039/b905642d

Dynamic nuclear polarization of water by a nitroxide radical: rigorous treatment of the electron spin saturation and comparison with experiments at 9.2 Tesla

Deniz Sezer, Marat Gafurov, M. J. Prandolini, Vasyl P. Denysenkov and Thomas F. Prisner*

Received 2nd April 2009, Accepted 15th June 2009
First published as an Advance Article on the web 6th July 2009
DOI: 10.1039/b906719c

The interaction between nuclear and electronic spins is of interest for structural characterization of biomolecules and biomedical imaging based on nuclear magnetic resonance. The polarization of the nuclear spins can be increased significantly if the electron spin polarization is kept out of equilibrium. We employ semiclassical relaxation theory to analyze the electronic polarization of the two-spin system characteristic of nitroxide radicals. Atomistic molecular dynamics simulations of the nitroxide TEMPOL in water are performed to account for the effects of tumbling and spin-rotation coupling on the spin–spin and spin–lattice relaxation times. Concentration effects on the electron saturation are introduced by allowing for Heisenberg spin exchange between two nitroxides. Polarization enhancement profiles, calculated from the computed saturation, are directly compared with liquid-state dynamic nuclear polarization experiments conducted at 260 GHz/400 MHz. The contribution of the separate hyperfine lines to the saturation can be easily disentangled using the developed formalism.

I. Introduction

The dynamic polarization of nuclear spins by paramagnetic species can lead to nuclear magnetizations which are significantly larger than their values in the absence of the polarizing agent. Undoubtedly, enhancement of the nuclear polarization is of direct potential significance for the characterization of large biomolecules using nuclear magnetic resonance (NMR) and for biomedical applications in which small organic molecules are detected using magnetic resonance imaging (MRI). From that perspective, it becomes highly desirable to develop the necessary technology for performing DNP under conditions appropriate for biomolecular NMR, namely at high magnetic fields and in aqueous solutions.

The first liquid-state DNP experiments at 3.4 and 9.2 Tesla have reported enhancements as large as −20 and −11, respectively, for the nuclear magnetization of water protons by small nitroxide radicals.[1,2] These results indicate that enhancements of significant practical interest are achievable even at such high fields. To appreciate the importance of the obtained DNP enhancements let us remember that the enhancement ε can be written as[3]

$$\varepsilon = \xi s f \gamma_e/\gamma_n, \quad (1)$$

where γ_e and γ_n are the electronic and nuclear magnetogyric ratios, ξ is the coupling factor of the two spins, s is the saturation factor of the electronic spins, and f is the leakage factor reflecting the faster nuclear relaxation in the presence of the electronic spins. Since the magnitudes of ξ, s and f are smaller than or equal to one, DNP enhancements of up to 660 are possible for protons. When the electron-nuclear coupling is dipolar, as in the case we are interested in, the coupling factor is at most 1/2 and the maximum possible DNP enhancement is −330. Unfortunately, this value is reachable only at low magnetic fields. The coupling factor decreases dramatically with increasing magnetic field. Whether it drops to essentially zero at magnetic fields of interest to high-resolution biomolecular NMR (*i.e.*, about 10 T) depends on the presence or absence of random molecular motions on a sub-picosecond time scale.

In the previous paper (I; DOI: 10.1039/b905709a) we used molecular dynamics (MD) simulations to calculate the coupling factors as a function of field strength for the water-TEMPOL system studied experimentally at 3.4 and 9.2 T. As expected, the coupling factors do decrease significantly with increase in the magnetic field. Nevertheless, our results show the presence of substantial sub-picosecond dynamics, in agreement with the experimentally observed enhancements. In fact, the coupling factors calculated from MD at 3.4 and 9.2 T are in excellent agreement with the values estimated from relaxation dispersion experiments.[1,2] Furthermore, according to the MD results, even at 12.8 T one can expect 70% of the enhancement observed at 9.2 T for TEMPOL in water (assuming the same saturation).

In the present paper we turn our attention to the saturation factor. Recently, a ''new model'' was developed to calculate the saturation factor of nitroxide radicals under liquid-state DNP conditions where the polarization mechanism is described by the Overhauser effect.[4] The model takes into account the effects of nitrogen nuclear spin relaxation

Institut für Physikalische und Theoretische Chemie, J. W. Goethe-Universität, 60438 Frankfurt am Main, Germany. E-mail: prisner@chemie.uni-frankfurt.de

(pertinent to nitroxide radicals) and Heisenberg spin exchange (relevant at the increased radical concentrations used in DNP experiments).[4] Explicitly considered is the master equation for the 12 *polulations* of the three-spin system electron–nitrogen–proton involved in the DNP phenomenon.[4] The formalism has been applied to determine the saturation factors at 9.8 GHz, and thus deduce coupling factors from the measured DNP enhancements, for a number of biological systems including micelles, vesicles, and proteins.[5,6]

Being limited to the relaxation dynamics of the populations, an inherent feature of this formalism is the lack of spin–spin (T_2) relaxation effects which operate on the spin *coherences*. Consequently, the dependence of the saturation on the microwave frequency ω (as opposed to the amplitude B_1) is also lacking. In the present article, the problem of calculating the electron spin saturation for given experimental conditions is revisited. In contrast to ref. 4, we consider the density matrix for the two-spin system electron–nitrogen, characteristic of nitroxide radicals. Neglecting the effect of the proton nuclear spins on the electron spin relaxation is common in the treatment of Overhauser-based DNP since other relaxation mechanisms are much stronger and dominate.[3]

The treatment of saturation and exchange effects in electron spin resonance (ESR) spectra of nitroxides has a long history.[7–9] Therefore, it is important to emphasize that our analysis of the electron spin saturation is not new in content. The generalization of the familiar Bloch equations to the two-spin system of interest [eqn (26)], however, is in a form that is particularly suitable for analyzing experimental DNP/ESR data and should be of broad interest.

Our ultimate goal in the present paper is to calculate DNP enhancements and compare directly with experiments at 9.2 T.[2,10] To this end, the coupling factor (calculated from MD simulations in paper I), is combined with the saturation factor, the calculation of which is the subject of the present work, using eqn (1). As already mentioned, a central role in our treatment of the saturation factor is played by the density matrix of the electron–nitrogen spin system. Within the approximations of the semiclassical theory of spin relaxation,[11,12] it is possible to rigorously account for the effect of the experimental conditions on the evolution of the density matrix, and thus calculate the saturation. The factors reflecting the experimental situation which are explicitly considered in this study are the spin–lattice and spin–spin relaxation times, T_1 and T_2, the rate of Heisenberg spin exchange, $1/\tau_H$, and the frequency and magnitude of the applied microwave field, ω and B_1. One of our main objectives is to demonstrate how all of these experimental parameters can be easily incorporated into the calculations.

The input that is necessary for the calculation of the saturation factor are the values of the magnetic tensors, the times T_1, T_2, and τ_H, as well as the magnitude and frequency of the microwave field. Ideally, knowledge about these parameters should come from independent experimental measurements. For example, direct access to T_2 processes is offered by continuous-wave (cw) ESR spectra. Similarly, the rate of Heisenberg spin exchange is accessible through line shape analysis of the cw-ESR spectra.[13,14] Also, the cw spectra in solution and frozen samples provide information about the magnetic g and A tensors. On the other hand, pulse ESR methods are typically employed to measure T_1 of nitroxides in aqueous samples.[15–17] Similarly, the amplitude B_1 of the microwave field in the cavity of the spectrometer is best quantified by measuring the duration of a 90° (π) pulse. To reiterate, the approach outlined in the present paper is concerned with utilizing all this independently available information to calculate the saturation factor under the given experimental conditions.

At the high magnetic field of interest for this work, there is one major stumbling block in putting the proposed formalism to work. Due to the experimental limitations at 260 GHz, there is no independently measured T_1 against which our calculations can be calibrated. Furthermore, the amplitude of the microwave field is not known exactly. As a result, the values of T_1 and B_1 that we use to calculate the saturation are estimated. However, that should not deflect from the main aim of the paper, which is to present a general and sound approach for calculating electron spin saturation under given experimental conditions in a form convenient to use in the context of DNP experiments.

Finally, a few words should be said regarding the spin–lattice and spin–spin relaxation mechanisms affecting the relaxation times T_1 and T_2. In the present paper, we explicitly account for three relaxation mechanisms: g-tensor anisotropy, electron-nuclear hyperfine coupling, and spin-rotation.[18,19] The time scales of the physical motions that lead to these mechanisms are extracted from atomistic MD simulations, similar to the ones employed in paper I. Other T_1 and T_2 relaxation mechanisms,[20] like hyperfine coupling to nitroxide protons, relaxation due to residual oxygen, g-strain broadening, or generalized spin-diffusion[19] are not treated explicitly. Such processes are accounted for by introducing additional exponential (Lorentzian) relaxation times, T_1^L and T_2^L, in order to obtain quantitative agreement with experimental cw-ESR spectra or T_1 values (if available). Since these additional parameters are used to calibrate T_1 and T_2 against independent experimental information, they do not constitute free (*i.e.*, arbitrary) parameters in the calculation of the electron spin saturation.

The article is organized as follows. In the next section the theoretical treatment of the electron spin saturation under DNP conditions is presented. The calculation of the saturation and the cw-ESR spectrum is formulated as the solution of a single matrix equation, in the spirit of the Bloch equations for spin 1/2. Brief description of the high-field ESR and DNP experiments is given in section III, which also contains details about the MD simulations. The results obtained by applying the formalism to DNP at 9.2 T together with a discussion of the implications are presented in section IV. The final section contains our concluding remarks.

II. Theory

A The spin Hamiltonian

We consider the following spin Hamiltonian (in units of angular frequency)

$$\hat{H}(t) = \hat{Z}(t) + \hat{W}(t) + \hat{N}(t) + \hat{L}(t), \qquad (2)$$

where

$$\hat{Z}(t) = |\gamma_e|\boldsymbol{B}_0\cdot\mathsf{G}(t)\cdot\hat{\boldsymbol{S}} \quad (3)$$

accounts for the Zeeman interaction of the electronic spin with the constant magnetic field $\boldsymbol{B}_0$;

$$\hat{W}(t) = |\gamma_e|\boldsymbol{B}_1(t)\cdot\mathsf{G}(t)\cdot\hat{\boldsymbol{S}} \quad (4)$$

contains the interaction with the microwave field $\boldsymbol{B}_1$;

$$\hat{N}(t) = |\gamma_e|\hat{\boldsymbol{I}}\cdot\mathsf{A}(t)\cdot\hat{\boldsymbol{S}} \quad (5)$$

accounts for the hyperfine interaction of the electronic and nuclear (^{14}N or ^{15}N) spins; and

$$\hat{L}(t) = -\boldsymbol{\eta}(t)\cdot\mathsf{T}(t)\cdot\hat{\boldsymbol{S}} \quad (6)$$

represents the coupling of the electronic spin to the mechanical angular momentum of the nitroxide molecule. In these expressions, $\hat{\boldsymbol{S}}$ and $\hat{\boldsymbol{I}}$ are the electronic and nuclear spin operators for the spin system on the nitroxide, γ_e is the gyromagnetic ratio of a free electron, $\boldsymbol{\eta}(t)$ is the angular velocity of the nitroxide moiety, $\mathsf{A}(t)$ is the hyperfine tensor (expressed in units of magnetic field),

$$\mathsf{G}(t) = \mathsf{g}(t)/g_e \quad (7)$$

is the electronic g-tensor, $\mathsf{g}(t)$, divided by the free electron g-factor, g_e,

$$\mathsf{T}(t) = \mathsf{g}(t) - g_e\mathsf{E} \quad (8)$$

is the spin-rotation coupling tensor, and E is the 3×3 identity matrix.

The coupling tensors G, A and T are typically diagonal in the same coordinate frame attached to the nitroxide. Their explicit time dependence in the equations above is due to the dynamics of this frame with respect to the stationary laboratory frame in which the constant external magnetic field $\boldsymbol{B}_0 = (0,0,B_0)$ is applied. Since the electronic spin is quantized in the laboratory frame, all the vector and tensor components in the Hamiltonian are with respect to it. The (circularly polarized) microwave magnetic field in the laboratory frame is given by $\boldsymbol{B}_1(t) = B_1(\cos\omega t, \sin\omega t, 0)$.

The spin-rotation coupling is included in the Hamiltonian because it provides an effective mechanism for spin–lattice relaxation. The nuclear quadrupole (for ^{14}N) interaction as well as the interactions with the nearby solvent or nitroxide proton nuclei is assumed to be negligible. The nuclear Zeeman interaction has not been shown in (2). However, within the approximations outlined below, it drops out of the analysis if only electronic spin observables are considered, as will be the case. (See *e.g.*, ch. 9 of ref. 21.)

To separate the isotropic and anisotropic parts we introduce

$$\begin{aligned} &G_0 = \mathrm{Tr}\{\mathsf{G}\}/3,\ A_0 = \mathrm{Tr}\{\mathsf{A}\}/3,\ T_0 = \mathrm{Tr}\{\mathsf{T}\}/3 \\ &\mathsf{G}' = \mathsf{G} - G_0\mathsf{E},\ \mathsf{A}' = \mathsf{A} - A_0\mathsf{E},\ \mathsf{T}' = \mathsf{T} - T_0\mathsf{E} \end{aligned} \quad (9)$$

where Tr{X} denotes the trace of X. In addition, we define the angular frequencies

$$\omega_0 = |\gamma_e|B_0G_0,\ \omega_1 = |\gamma_e|B_1G_0,\ \omega_A = |\gamma_e|A_0, \quad (10)$$

the first of which is the electron Larmor precession frequency. All this allows us to write

$$\begin{aligned} &\hat{Z}_0 = \omega_0\hat{S}_z,\ \hat{N}_0 = \omega_A\hat{\boldsymbol{I}}\cdot\hat{\boldsymbol{S}}, \\ &\hat{W}_0(t) = \tfrac{1}{2}\omega_1(e^{i\omega t}\hat{S}_- + e^{-i\omega t}\hat{S}_+) \end{aligned} \quad (11)$$

for the parts which are independent of the orientation of the nitroxide, and

$$\begin{aligned} &\hat{Z}_1(t) = |\gamma_e|\boldsymbol{B}_0\cdot\mathsf{G}'(t)\cdot\hat{\boldsymbol{S}},\ \hat{N}_1(t) = |\gamma_e|\hat{\boldsymbol{I}}\cdot\mathsf{A}'(t)\cdot\hat{\boldsymbol{S}}, \\ &\hat{W}_1(t) = |\gamma_e|\boldsymbol{B}_1\cdot\mathsf{G}'(t)\cdot\hat{\boldsymbol{S}} \end{aligned} \quad (12)$$

for the orientation dependent parts. We also write $\hat{L} = \hat{L}_1 + \hat{L}_2$, where

$$\hat{L}_1(t) = -T_0\boldsymbol{\eta}(t)\cdot\hat{\boldsymbol{S}},\ \hat{L}_2(t) = -\boldsymbol{\zeta}(t)\cdot\hat{\boldsymbol{S}}, \quad (13)$$

and $\boldsymbol{\zeta}(t) = \boldsymbol{\eta}(t)\cdot\mathsf{T}'(t)$. Note that both $\hat{L}_1$ and $\hat{L}_2$ dependent on the orientation of the nitroxide with respect to the external magnetic field.

B Semiclassical relaxation

For a detailed discussion of the assumptions behind semiclassical relaxation theory the reader should consult the existing literature.[11,12] Here we would only like to point out that the radicals are assumed to tumble sufficiently fast such that complete ensemble averaging is experienced by each one of them over periods much shorter than the spin–spin and spin–lattice relaxation times. The coherent spin evolution is then driven by the rotationally invariant, average Hamiltonian. Spin relaxation, on the other hand, is caused by second-order terms in the anisotropic part of the Hamiltonian. In the coordinate frame that rotates about the laboratory z-axis with angular frequency ω, these isotropic and anisotropic Hamiltonians are, respectively,

$$\hat{H}'_0 = (\Omega_0 + \omega_A\hat{I}_z)\hat{S}_z + \tfrac{1}{2}\omega_1(\hat{S}_+ + \hat{S}_-), \quad (14)$$

and

$$\hat{H}'_1 = \hat{Z}'_1(t) + \hat{W}'_1(t) + \hat{N}'_1(t) + \hat{L}'(t), \quad (15)$$

after neglecting the non-secular terms. Here, prime refers to the rotating frame and $\Omega_0 = \omega_0 - \omega$ is the relative Larmor frequency. For the density matrix in the rotating frame, $\rho(t)$, which describes the quantum mechanical state of the spin system on the nitroxide, a relaxation equation is derived.[11] It reads

$$\dot{\rho}(t) = -i[\hat{H}'_0,\rho(t)] - R(\rho(t) - \rho^{eq}), \quad (16)$$

where the dot above ρ stands for $\mathrm{d}/\mathrm{d}t$, $[\cdot,\cdot]$ is a commutator, ρ^{eq} is the density matrix at thermal equilibrium, and R is a relaxation (super)operator which acts on the deviation of $\rho(t)$ from equilibrium. The relaxation operator is given by

$$R(\cdot) = \int_0^\infty \mathrm{d}\tau[\overline{\hat{H}'_1(t)},[\hat{H}'_1(t-\tau)],\cdot]], \quad (17)$$

where the line denotes ensemble and time average.

In principle, the relaxation kernel contains all the 16 pairwise combinations of the four terms in eqn (15). Typically, $\hat{W}'_1$ is small and its effect on relaxation can be neglected.

Because the fluctuations of the angular velocity $\boldsymbol{\eta}$ are much faster than the time scale of molecular tumbling, the cross-correlations of the spin-rotation coupling with all the other terms vanish.[22] This leaves us with the following contributions to relaxation:

$$R(\cdot) = R_{ZZ}(\cdot) + R_{ZN}(\cdot) + R_{NN}(\cdot) + R_{LL}(\cdot), \qquad (18)$$

where the subscripts indicate the pair of operators that appear in the kernel of eqn (17).

To simplify the calculations of these relaxation operators the nitroxide is assumed to undergo isotropic rotational diffusion. This approximation is expected to apply for TEMPOL and other small nitroxides. (If suspected to play a role, the contribution due to anisotropic diffusion can be easily included in the present analysis.[18]) Expressions for each term on the right hand side of eqn (18) are given in eqn (A1) under the assumption that effects of dynamic frequency shift[23] are negligible, thus considering only the real parts of the spectral densities. Also, the nuclear Zeeman and hyperfine frequencies (on the order of tens of MHz) have been neglected in comparison with the frequencies of electron spin precession (tens or hundreds of GHz) or set equal to zero when appearing in the spectral densities associated with molecular tumbling and spin-rotation coupling. These assumptions are justified in the fast motional regime in which the Redfield theory is applicable.[21]

C Relaxation equation of motion

For easier access to the electronic spin observables, like the saturation and the cw-ESR spectrum, we write the density matrix as

$$\rho(t) = \rho_0(t)\hat{S}_0 + \rho_z(t)2\hat{S}_z + \rho_+(t)\hat{S}_- + \rho_-(t)\hat{S}_+, \quad (19)$$

where each of the submatrices ρ_κ, $\kappa = 0, z, +, -$ is a 3×3 ($I = 1$) or a 2×2 ($I = 1/2$) matrix. The density matrix from eqn (19) can be inserted into eqn (A1) to calculate the relaxation of the separate ρ_κs. The resulting expressions are presented in the appendix together with the expressions for the coherent evolution under the Hamiltonian $\hat{H}'_0$ [eqn (A8) to (A12)].

The longitudinal and transverse electronic magnetizations, necessary for the calculation of the steady-state saturation and the cw-ESR spectrum, can be determined from the density matrix according to

$$\begin{aligned} \langle \hat{S}_z \rangle(t) &= \mathrm{Tr}\{\hat{S}_z \rho(t)\} = \mathrm{Tr}\{\rho_z(t)\}, \\ \langle \hat{S}_+ \rangle(t) &= \mathrm{Tr}\{\hat{S}_+ \rho(t)\} = \mathrm{Tr}\{\rho_+(t)\}. \end{aligned} \qquad (20)$$

In either case, only the entries along the main diagonal of ρ_z and ρ_+ are necessary. Interestingly, neither the relaxation operators nor the coherent evolution couple the diagonal elements of the submatrices ρ_κ to their off-diagonal elements. Thus, it is possible to calculate the evolution of the diagonal entries only, which are coupled to each other. In the following, we limit our attention to these elements (to be denoted by $[\rho_\kappa]_{m,m}$, with $m = 1,0,-1$ for $I = 1$, and $m = 1/2, -1/2$ for $I = 1/2$) and completely disregard the rest.

It is convenient to arrange the elements $[\rho_\kappa]_{m,m}$ in column vectors as follows:

$$\sigma_k = \begin{bmatrix} [\rho_k]_{1,1} \\ [\rho_k]_{0,0} \\ [\rho_k]_{-1,-1} \end{bmatrix} \text{ and } \sigma_k = \begin{bmatrix} [\rho_k]_{1/2,1/2} \\ [\rho_k]_{-1/2,-1/2} \end{bmatrix}, \qquad (21)$$

where the former corresponds to $I = 1$ and the latter to $I = 1/2$. With that understanding, the relaxation equation of motion (16) becomes

$$\begin{bmatrix} \dot{\sigma}_+ \\ \dot{\sigma}_- \\ \dot{\sigma}_z \\ \dot{\sigma}_0 \end{bmatrix} = (-\mathrm{i}\mathscr{L} - \mathscr{R}) \begin{bmatrix} \sigma_+ \\ \sigma_- \\ \sigma_z \\ \sigma_0 \end{bmatrix} + \mathscr{R} \begin{bmatrix} 0 \\ 0 \\ \sigma_z^{\mathrm{eq}} \\ 0 \end{bmatrix}, \qquad (22)$$

for the 12×1 ($I = 1$) or 8×1 ($I = 1/2$) column vector constructed by stacking the column vectors σ_κ on top of each other as shown. The (12×12 or 8×8) matrices $\mathscr{L}$ and $\mathscr{R}$ contain the contribution of the coherent evolution and the relaxation, respectively. These are found to be

$$\mathscr{L} = \begin{bmatrix} -\Omega_0 \mathbb{I}_0 - \omega_A \mathbb{I}_z & 0 & \omega_1 \mathbb{I}_0 & 0 \\ 0 & \Omega_0 \mathbb{I}_0 + \omega_A \mathbb{I}_z & -\omega_1 \mathbb{I}_0 & 0 \\ \frac{1}{2}\omega_1 \mathbb{I}_0 & -\frac{1}{2}\omega_1 \mathbb{I}_0 & 0 & 0 \\ 0 & 0 & 0 & 0 \end{bmatrix} \qquad (23)$$

and

$$\mathscr{R} = \begin{bmatrix} \mathbb{R}_2 & & & \\ & \mathbb{R}_2 & & \\ & & \mathbb{R}_1 & \mathbb{U} \\ & & \mathbb{V} & \mathbb{R}_0 \end{bmatrix} + \frac{1}{\tau_{\mathrm{H}}} \begin{bmatrix} \mathbb{X} & & & \\ & \mathbb{X} & & \\ & & \mathbb{X} & \\ & & & 0 \end{bmatrix}, \qquad (24)$$

where each of the explicitly written entries is a 3×3 or 2×2 matrix and the elements left empty are equal to zero. The matrix $\mathbb{I}_z$ has the same matrix representation as the (three- or two-dimensional) nuclear spin operator $\hat{I}_z$. We use a different symbol since $\mathbb{I}_z$ acts only on the diagonal entries $[\rho_\kappa]_{m,m}$. In the same way, the matrices $\mathbb{I}_+$ and $\mathbb{I}_-$ are understood to have the same matrix representations as $\hat{I}_+$ and $\hat{I}_-$. The representations of $\mathbb{R}_1$, $\mathbb{R}_2$, $\mathbb{R}_0$, $\mathbb{U}$, $\mathbb{V}$, and $\mathbb{X}$, which depend on whether we deal with $I = 1$ or $I = 1/2$, are given in the appendix for each of these two cases. The last relaxation matrix in eqn (24) accounts for Heisenberg spin exchange, characterized by the exchange time scale τ_{H}, and considered in more detail in the appendix.

Two things need to be mentioned regarding eqn (22) before using it in numerical work. The first pertains to the fact that the submatrix ρ_0 contains the identity matrix, $\hat{I}_0$, along its main diagonal. (This is the part $\hat{I}_0\hat{S}_0$ in the full density matrix ρ.) Since this part is not affected by the relaxation or the coherent evolution, it poses numerical problems during the matrix inversion necessary to calculate the steady-state solution (see next paragraph). However, this part of the density matrix does not deviate from its equilibrium value. Therefore, it can be completely disregarded. How we do so is discussed in the appendix. As a result, $\mathbb{R}_0$ becomes a 2×2 matrix when $I = 1$, or a scalar when $I = 1/2$. Similarly, $\mathbb{U}$ and $\mathbb{V}$ turn into 3×2 and 2×3 ($I = 1$), or 2×1 and 1×2 ($I = 1/2$) matrices.

Second, instead of dealing with the complex matrix $\mathrm{i}\mathscr{L}$ in eqn (22) one can introduce

$$\sigma_x = (\sigma_+ + \sigma_-)/2, \; \sigma_y = (\sigma_+ - \sigma_-)/2\mathrm{i}, \qquad (25)$$

and rewrite the relaxation equation of motion as

$$\dot{\boldsymbol{\sigma}} = (\mathscr{K} - \mathscr{R})\boldsymbol{\sigma} + \mathscr{R}\boldsymbol{\sigma}^{\mathrm{eq}}, \tag{26}$$

where

$$\boldsymbol{\sigma} = [\sigma_x,\sigma_y,\sigma_z,\sigma_0],\ \boldsymbol{\sigma}^{\mathrm{eq}} = [0,0,\sigma_z^{\mathrm{eq}},0] \tag{27}$$

are column vectors, $\mathscr{R}$ is the same as before, and

$$\mathscr{K} = \begin{bmatrix} 0 & -\Omega_0\mathbb{I}_0 - \omega_A\mathbb{I}_z & 0 & 0 \\ \Omega_0\mathbb{I}_0 + \omega_A\mathbb{I}_z & 0 & -\omega_1\mathbb{I}_0 & 0 \\ 0 & \omega_1\mathbb{I}_0 & 0 & 0 \\ 0 & 0 & 0 & 0 \end{bmatrix}. \tag{28}$$

We prefer this latter form. Eqn (26) is a natural generalization of the familiar Bloch equations to the electron-nuclear spin system on the nitroxide.

D The saturation, the cw-ESR spectrum, and T_1

Both the saturation factor and the cw-ESR spectrum are obtained under steady-state conditions. The steady-state solution of eqn (26) is

$$\boldsymbol{\sigma}^{\mathrm{ss}} = (\mathscr{R} - \mathscr{K})^{-1}\mathscr{R}\boldsymbol{\sigma}^{\mathrm{eq}}. \tag{29}$$

In the appendix, this solution is examined in more detail and its correspondence to the steady-state solution of the Bloch equations is illustrated.

The separate contributions of the hyperfine lines to the steady-state saturation can be read from the corresponding entries of the vector σ_z^{ss}, whose sum gives the total longitudinal magnetization. Similarly, the contribution of each ESR line to the dispersion and absorption components of the cw-ESR spectrum are contained in the corresponding element of σ_x^{ss} and σ_y^{ss}, respectively. The sum over the hyperfine lines gives the observed spectral line shape.

For direct comparison with experiment it is preferable to calculate a cw spectrum in derivative form. Analytically, this can be achieved by differentiating $\boldsymbol{\sigma}^{\mathrm{ss}}$ with respect to the microwave frequency:

$$\frac{\partial\boldsymbol{\sigma}^{\mathrm{ss}}}{\partial\omega} = (\mathscr{R} - \mathscr{K})^{-1}\frac{\partial\mathscr{K}}{\partial\omega}(\mathscr{R} - \mathscr{K})^{-1}\mathscr{R}\boldsymbol{\sigma}^{\mathrm{eq}}. \tag{30}$$

In contrast to the saturation and the cw spectrum, the relaxation time T_1 cannot be obtained from the steady-state solution (29). For its calculation we go back to eqn (26). We have in mind a saturation recovery experiment where the (longitudinal) magnetization is fully destroyed at $t = 0$ and its recovery is observed for later times. Since $\omega_1 = 0$ in this case, the evolution of σ_z can be followed by solving the simpler equation

$$\begin{bmatrix} \dot{\sigma}_z \\ \dot{\sigma}_0 \end{bmatrix} = -\begin{bmatrix} \mathbb{R}_1 & \mathbb{U} \\ \mathbb{V} & \mathbb{R}_0 \end{bmatrix}\left(\begin{bmatrix} \sigma_z \\ \sigma_0 \end{bmatrix} - \begin{bmatrix} \sigma_z^{\mathrm{eq}} \\ 0 \end{bmatrix}\right), \tag{31}$$

subject to the initial condition $[\sigma_z(0),\sigma_0(0)] = 0$. The solution is readily found to be

$$\begin{bmatrix} \sigma_z(t) \\ \sigma_0(t) \end{bmatrix} = \left(1 - \exp\left(-\begin{bmatrix} \mathbb{R}_1 & \mathbb{U} \\ \mathbb{V} & \mathbb{R}_0 \end{bmatrix}t\right)\right)\begin{bmatrix} \sigma_z^{\mathrm{eq}} \\ 0 \end{bmatrix}. \tag{32}$$

Using it, the recovery of the longitudinal magnetization is calculated by performing the following dot product

$$\langle\hat{S}_z\rangle(t) = [1,1,1,0,0]\begin{bmatrix} \sigma_z(t) \\ \sigma_0(t) \end{bmatrix}. \tag{33}$$

Fitting the evolution of $\langle\hat{S}_z\rangle$ to a monoexponential allows us to obtain the spin–lattice relaxation time T_1.

III. Methods

A ESR and DNP experiments at 9.2 T

The DNP experiments at 9.2 T were performed using a double-resonance structure, which allows for simultaneous ESR and NMR excitations at 260 GHz/400 MHz.[24] Accurate direct determination of the microwave B_1 by measuring a π (90°) pulse could not be established at 260 GHz. An estimate of the maximum B_1 of 1.6 G was achieved using a high-frequency structure simulator.[24] Since the simulation represents an ideal structure, B_1 is expected to be smaller in reality because of geometrical imperfections and non-ideal surface resistance of the hand-made structure. In addition, small changes of B_1 with frequency, resulting from power fluctuations within the 260 GHz microwave source and standing waves within the transmission system, cannot be ruled out. Due to the small size of the microwave cavity, exact reproduction of the sample position or of the cavity dimensions (when tuning the cavity by adjusting its length) is difficult to achieve.

When DNP enhancements were experimentally acquired under maximum available microwave power the sample was observed to heat up and reach a steady temperature, which was determined to be about 20 °C above the ambient room temperature by measuring the shift of the NMR line of the water protons.[2,10] Therefore, when comparing with the measured DNP enhancement we use physical parameters appropriate for $T \approx 40$ °C. The relaxivity at this elevated temperature was measured to be $k = 0.09\ \mathrm{s^{-1}mM^{-1}}$, and the T_1 of pure water, $T_{1\mathrm{w}}$, was measured to be 4.8 s. The leakage factor for a given nitroxide concentration c (mM) is calculated from $f(c) = kcT_{1\mathrm{w}}/(1 + kcT_{1\mathrm{w}})$. In section IV we use the following three leakage factors:

$$f(3.15) = 0.576,\ f(4.2) = 0.645,\ f(6.3) = 0.731, \tag{34}$$

determined from this expression.

B Computational details

The simulated system was a cubic box filled with TIP3P[25] waters and one TEMPOL molecule. The force field parameters used for the nitroxide were from ref. 26. The simulations were performed with NAMD,[27] at constant volume and temperature (NVT ensemble), using periodic boundary conditions. Electrostatic interactions were treated with particle mesh Ewald.[28] Bonds involving hydrogen atoms were constrained with SETTLE[29] and a 2 fs time step was used for the numerical integration.

To properly account for the heating of the sample, MD simulations were performed at three different temperatures, $T = 298$ K (25 °C), 308 K (35 °C), and 318 K (45 °C). The

temperature was controlled with a Langevin thermostat coupled to the heavy atoms only. Different Langevin friction was used at the different temperatures such that the simulated water diffusion matches the experimental values. (See paper I for more details on this point.) In paper I TEMPOL–water coupling factors were calculated as a function of applied magnetic field for the three temperatures. In these simulations the system contained 2991 waters in addition to a single TEMPOL molecule. The calculated coupling factors at 260 GHz, of interest to the present study, were obtained to be $\xi(25\ ^\circ\mathrm{C}) = 1.80\%$, $\xi(35\ ^\circ\mathrm{C}) = 2.43\%$, and $\xi(45\ ^\circ\mathrm{C}) = 2.97\%$. When comparing with experimental DNP enhancement data in section IV we use $\xi = 2.7\%$, which is intended to correspond to the value at 40 °C.

In the next section we calculate T_1 and T_2 relaxation times for TEMPOL from the correlation functions of its rotational displacement and angular velocity. Such correlation functions of TEMPOL only contain more sampling noise compared to the TEMPOL–water correlation functions, because there is a single TEMPOL molecule in the simulation box as opposed to thousands of water molecules which contribute to the statistical averaging. To obtain better estimates of the rotational time scale τ_D we performed another set of simulations like the ones described in paper I but containing one TEMPOL molecule in a smaller box with 991 waters instead of 2991. (The initial water boxes contained 1000 and 3000 waters, respectively, and 9 waters were removed after introducing the nitroxide.) Reducing the system size is permissible when only the rotational dynamics of TEMPOL is of interest. As in paper I, the simulations lasted for 2.1 ns, coordinates were saved every 0.15 ps, and the first 90 ps were excluded from the analysis. These new trajectories were analyzed together with the trajectories of the larger system, reported in paper I, thus doubling the amount of sampling.

Lastly, angular velocity correlation functions are necessary to calculate the effect of spin-rotation coupling on T_1 and T_2. Since the angular velocity decorrelates extremely fast MD snapshots were saved every 20 fs to resolve this rapid decay. This was done by extending the previous simulations for additional 600 ps and saving the coordinates every 10 integration steps (instead of every 75). To calculate an instantaneous angular velocity it is necessary to definite a rigid coordinate frame attached to the nitroxide. However, because the angular velocity correlation time, which was found to span only tens of femtoseconds (*cf.* section IV), is comparable with the time scales of internal molecular vibrations, defining a *rigid* molecular frame becomes problematic. It should be remembered that, if treated quantum mechanically, vibrational modes with frequency of about 200 cm^{-1} and higher (period of 150 fs and smaller) should not be excited at all at room temperature. This is certainly not true for the classical MD simulations at hand. Such fast molecular vibrations not only prevent the clear-cut definition of a body-fixed coordinate frame but also contaminate the correlation function of the angular velocity with spurious oscillations. In an effort to reduce these unwanted effects we have defined a body-fixed frame using the nitroxide oxygen, nitrogen and the four carbon atoms on the ring which are closest to the nitrogen atom.

IV. Results and discussion

A Rotational correlation functions

1 Angular displacement. To calculate the time scale of rotational diffusion, τ_D, three orthogonal vectors were defined on the nitroxide. For each of these vectors $\boldsymbol{r} = (r_x, r_y, r_z)$ the auto-correlation of the following three functions was calculated:

$$f_i(\boldsymbol{r}) = 1 - 3r_i^2/r^2,\ i = x,y,z. \tag{35}$$

Due to rotational isotropy the correlation functions for the three choices of i are expected to be equal. This allowed us to take the average of the three correlation functions and obtain a better estimate. The average of the correlation functions over $i = x,y,z$ for the three vectors on the nitroxide are shown as thin lines in Fig. 1. Although the decays for the three vectors are not identical, thus indicating that the rotational dynamics of TEMPOL in water deviates slightly from isotropic diffusion, the latter is seen to be a rather good approximation. Therefore, a single tumbling time, τ_D, was calculated from the average of the correlation functions for the three orthogonal vectors (the thick lines in Fig. 1). The average correlation functions were fit to a sum of two exponential decays in the range $\tau \in [0,50)$ ps. The time scales and amplitudes deduced from the fits are given in Table 1. The second decay, which is responsible for at most 9% of the total amplitude, was introduced to account for the initial fast decrease of the

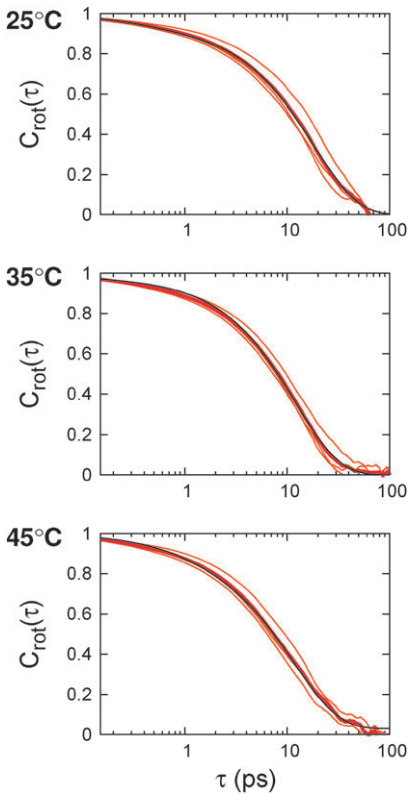

Fig. 1 Rotational correlation functions for three orthogonal vectors on TEMPOL (thin colored lines), the average correlation functions (thick colored lines) and the best exponential fits to the average (thin black lines).

Table 1 Rotational correlation times and corresponding amplitudes

	τ_D^{av}/ps	a_D	τ_{fast}/ps	a_{fast}
25 °C	18.1	0.94	0.4	0.06
35 °C	12.0	0.98	0.1	0.02
45 °C	11.8	0.88	1.1	0.09[a]

[a] The remaining amplitude of 0.03 was accounted for by an extremely slow decay on a practically infinite time scale.

orientational correlation function. The slower time scale was identified with the tumbling time.

On the basis of the obtained rotational correlation times we deduce that $\tau_D = 20$ ps should be used in the simulation of ESR data obtained at room temperature. For the simulation of data under DNP conditions, where the sample is measured to be 20 °C hotter than the ambient temperature, we use $\tau_D = 12$ ps.

2 Angular velocity

The angular velocity correlation functions were calculated from the shorter (600 ps) trajectories for which snapshots were saved for analysis every 10 integration steps. At every snapshot the rotation matrix that transforms the current body-fixed coordinate frame (defined as described above) to the frame in the next snapshot was extracted. These rotation matrices were used to calculate the axis and the angle of the rotation. The (instantaneous) angular velocities were obtained by dividing the angles of rotation by the time step.

The angular velocity correlation functions obtained from this procedure are shown in Fig. 2. The spikes which are visible in these correlation functions are not due to insufficient sampling but correspond to molecular vibration periods which have not been averaged out by the selection of the six atoms used to define a *rigid* molecular frame (see discussion in section III B). The raw correlation functions were fit to

$$C_{ang}(\tau) = a_1 e^{-\tau/\tau_1} + a_2 e^{-\tau/\tau_2} \cos(\tau/\tau_3). \quad (36)$$

The parameters yielding the best fit are given in Table 2. This analytical functional form leads to the following spectral density [*cf.* eqn (A7)]

$$J^{\eta+\zeta}(\omega) = (T_0^2 + T'^2)\left[\frac{a_1\tau_1}{1+\omega^2\tau_1^2} + \frac{a_2\tau_2/2}{1+(\omega-1/\tau_3)^2\tau_2^2} + \frac{a_2\tau_2/2}{1+(\omega+1/\tau_3)^2\tau_2^2}\right], \quad (37)$$

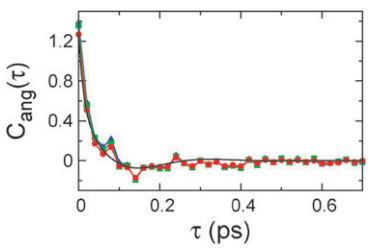

Fig. 2 Angular velocity correlation functions (symbols and lines) and the best fit for 25 °C (thin black line). Circles, squares and triangles correspond to 25, 35 and 45 °C, respectively.

Table 2 Time scales and amplitudes used to fit the angular velocity correlation functions calculated from the MD trajectories

	τ_1/fs	τ_2/fs	τ_3/fs	a_1/rad^2 ps^{-2}	$a_1 + a_2$[a]
25 °C	13.1	100.	56.1	0.893	1.267
35 °C	11.6	92.4	59.7	0.850	1.360
45 °C	11.7	92.8	64.9	0.860	1.389

[a] The sum $a_1 + a_2$ was restricted to $C_{ang}(0)$ during the fit.

which is used in the calculation of the relaxation rate matrices $\mathbb{R}_1$ and $\mathbb{R}_2$.

B Calibrating the input parameters

1 T_2 relaxation and cw-ESR spectra. The steady-state solution of the generalized Bloch equations, eqn (B4), can be used to calculate cw-ESR spectra. Such calculated spectra are shown in Fig. 3 and 4, where they are compared with experimental spectra recorded at 9.2 T (260 GHz). The data are for 0.6 mM aqueous solutions of ^{14}N and ^{15}N TEMPOL, respectively. Given the low radical concentration, the spectra were simulated without any Heisenberg exchange. As is typical when acquiring cw-ESR spectra, only weak microwave power was applied. Thus, any excess heating of the sample is not expected. The temperature therefore should be close to room temperature, implying a rotational tumbling rate of about 20 ps. Similarly, the spin-rotation parameters calculated from the MD simulations at 25 °C were employed.

As expected at such high magnetic fields, the width of the lines of the simulated spectra were found to be rather sensitive to the entries of the g tensor, in particular to its largest component g_{xx}, and less sensitive to the elements of the A tensor. The following literature values of the magnetic tensors were used in the calculation of the reported spectra:[15,30]

$$\mathsf{g} = \mathrm{diag}(2.0088, 2.006, 2.002),$$
$$\mathsf{A} = \mathrm{diag}(6.3, 6.3, 37.5)\ \mathrm{Gauss}. \quad (38)$$

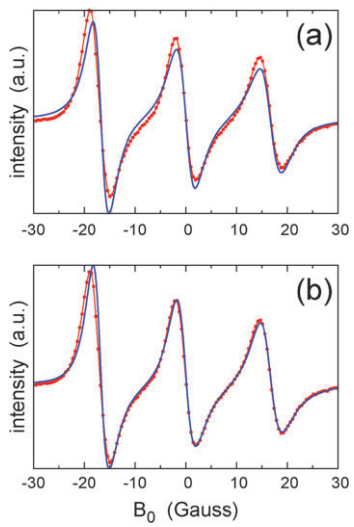

Fig. 3 Comparison of the experimental cw-ESR spectra (lines and points) with the calculated spectra (lines) for ^{14}N TEMPOL. (a) Pure absorption spectrum. (b) The absorption component in (a) minus 0.28 of the dispersive component.

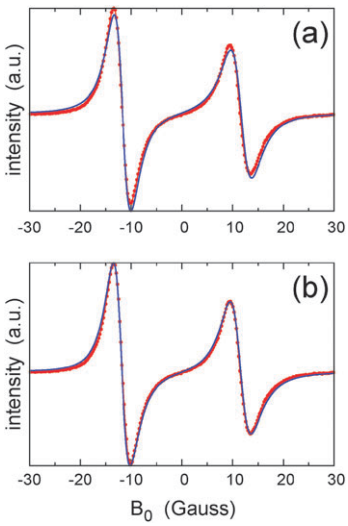

Fig. 4 Same as Fig. 3 for ^{15}N TEMPOL. In (b) the dispersive component is multiplied by 0.12 and subtracted from the pure absorption in (a).

The g_{xx} and A_{zz} values reflect the polar aqueous environment.[30] The A_{xx} and A_{yy} values, which are difficult to access precisely, were kept equal and chosen such that the frequency spacing between the hyperfine lines agrees with experiment. For the simulation of the ^{15}N spectra the hyperfine tensor was scaled by a factor of 1.4 to account for the difference in the magnitudes of the respective magnetogyric ratios.

The differential broadening of the hyperfine lines observed in the experiment is faithfully reproduced in the simulations. The differential broadening in the calculations is solely due to the relaxation mechanism described by the operators R_{ZN} and R_{NN} and is dominated by the tumbling time τ_D. However, to obtain the overall widths of the spectral lines shown in Fig. 3 and 4, additional broadening of 0.8 G had to be introduced. This was done by adding the corresponding (scalar) relaxation rate to the matrix $\mathbb{R}_2$. Including small broadenings in the quantitative simulation of cw-ESR spectra at high fields is not uncommon.[18,31–33] Residual oxygen or *g*-strain effects are thought to be responsible for this additional relaxation. Once again, the broadening introduced by hand is the same for all the three lines and does not contribute to the *differences* in the line widths. Thus, the tumbling deduced from MD is seen to account rather well for the differential T_2 relaxation of TEMPOL.

By definition, the calculated absorption spectra shown in Fig. 3(a) and 4(a) are symmetrically positioned with respect to the horizontal axis, such that the integral of the spectrum vanishes. Clearly, the experimental lines are shifted slightly upward in an asymmetric fashion. This points to the presence of small dispersive component that is difficult to completely get rid of experimentally at this high magnetic field. The spectra in Fig. 3(b) and 4(b) were simulated by subtracting some portion (0.28 for ^{14}N and 0.12 for ^{15}N) of the steady-state dispersion, σ_x^{ss}, from the absorption, σ_y^{ss}. As a result, perfect agreement with experiment was achieved. The characteristic way in which the addition of a dispersive component affects the cw spectrum is evident from the comparison of parts (a) and (b) of the two Figures. It should be clear that having the dispersive component in the experimental high-frequency spectra does not compensate for possible systematic errors in the spin–spin relaxation mechanisms, including the value of the rotational correlation time.

The parameters used in the simulation of the cw-ESR spectra in Fig. 3 and 4 are summarized in Table 3.

2 Choosing T_1 and the rate of Heisenberg spin exchange. The spin–lattice relaxation time, T_1, is another input parameter that has to be calibrated against independent experimental information. Unfortunately, T_1 data to compare with is not available at 260 GHz. The spin–lattice relaxation times for the nitroxide TEMPONE (which is similar to TEMPOL) in water have been published for frequencies up to 94 GHz.[16,17] The reported values are shown in Table 4. It is seen that up to 34.6 GHz T_1 increases with the field, after which it starts to decrease.

The next two columns in Table 4 show calculated T_1s. The T_1^D values are obtained by considering the effect of the nitroxide tumbling only (with correlation time τ_D = 20 ps). Including the spin-rotation coupling determined from the MD simulations at 25° leads to the values in the column $T_1^{D,sr}$. Clearly, the spin-rotation coupling is essential for calculating T_1 values in reasonable agreement with experiment. This is especially so at the higher frequencies, where the T_1^Ds are off by more than an order of magnitude.

Although spin-rotation coupling is essential, the coupling estimated from the MD simulations is not sufficient for quantitative agreement with experiment. This is not surprising, however, since other spin–lattice relaxation mechanisms, not explicitly accounted for in our treatment, are expected to be operational.[19] To account for their effect, a scalar relaxation rate can be added to the relaxation matrix $\mathbb{R}_1$. In fact, this additional relaxation can be varied until any desired T_1 is achieved. In column $T_{1,L}^{-1}$ of Table 4 we report the magnitudes of additional relaxation (in Gauss) that lead to final T_1^{calc} values in perfect agreement with experiment. The calculated value at 260 GHz is an arbitrary but reasonable projection of the trend that is seen in the experimental data.

Finally, before proceeding to the calculation of the saturation factor and the DNP enhancements, it is necessary to select the time scale of Heisenberg spin exchange. The rate of intermolecular spin exchange has been estimated as 2.2×10^9 M^{-1}s^{-1} for TEMPONE in benzene at room temperature.[34] (The power of 10 is −9 in ref. 34, but this must be a misprint.) For c = 3.15 mM this would imply τ_H = 144 ns. Taking the exchange rate to be inversely proportional to the viscosity of the solvent we can estimate the exchange rate in water as

Table 3 Parameters used in the simulation of the cw-ESR spectra in Fig. 3 and 4

B_0/G	B_1/G	τ_D/ps	$T_{2,L}^{-1}$/G	τ_H/ns	Disp.[a]
92123.8	0.001	20	0.8	∞[b]	0.28/0.12

[a] The dispersive component subtracted from the absorption for ^{14}N/^{15}N, respectively. [b] Intended to reflect the low concentration of c = 0.6 mM.

Table 4 Comparison of the calculated T_1 times (in ns, unless specified otherwise) with experiment

GHz	T_1^{exp}[a]	T_1^D/μs	$T_1^{D,sr}$	$T_{1,L}^{-1}$/G	T_1^{calc}
9.15	490	1.3	660	0.028	490
18.5	770	3.4	920	0.012	770
34.6	920	7.5	1100	0.01	920
93.8	880	14.6	1200	0.017	880
260	—	16.8	1200	0.02	850

[a] Experimental values for TEMPONE at 20 °C.[16,17]

τ_H = 220 ns. (The viscosities of water and benzene at 20 °C are, respectively, 1.00 and 0.652 cP.) In contrast to this number, the exchange rate of Fremy's salt in water at 67 °C was deduced to be 9.6×10^8 M^{-1} s^{-1} in ref. 13. This implies τ_H = 330 ns for c = 3.15 mM. In our case, τ_H is expected to be larger both because the translational diffusion coefficient of the bulkier TEMPOL radical should be smaller and because the temperature is lower. Considering that nitroxide radicals are polar, we suspect that the rate of their encounter and spin exchange in nonpolar solvents, like benzene and toluene, may be different than the rate in water (even after adjusting for differences in viscosity). On the other hand, the exchange rate measured in water is for Fremy's salt, which is a charged radical. Given these complications, we select τ_H = 400 ns to simulate the saturation factor but explicitly examine the effect of increasing the Heisenberg spin exchange rate by a factor of two (*i.e.*, τ_H = 200 ns).

C DNP enhancement and saturation

1 DNP enhancements. As discussed in section III, the DNP enhancements were obtained at $T \approx 40$ °C, which implies τ_D = 12 ps for the tumbling time (*cf.* Table 1) and ξ = 2.7% for the coupling factor. Also, we use the spin-rotation coupling parameters deduced from the MD simulation at 45 °C. The DNP enhancements calculated using f = 0.576 (the leakage factor for c = 3.15 mM) and Heisenberg spin exchange time of τ_H = 400 ns, in addition to the aforementioned parameters, are compared with experiment in Fig. 5 as a function of microwave frequency. (The simulation parameters are summarized in Table 5.) The agreement between theory and experiment is seen to be rather good. In particular, the width and height of each line is captured pretty well. As expected, the broader hyperfine line in the cw-ESR spectrum (on the right in Fig. 3) corresponds to the broader and smaller line in the

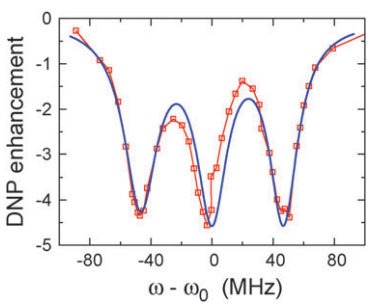

Fig. 5 Comparison of the calculated (line) and measured DNP (squares) enhancements at 260 GHz as a function of the microwave frequency.

Table 5 Parameters used in the simulation of the DNP enhancements in Fig. 5[a]

B_0/G	B_1/G	τ_D/ps	$T_{i,L}^{-1}$/G	c/mM	f	τ_H/ns
92123.8	0.9	12	0.8/0.02[b]	3.15	0.576	400

[a] ξ = 2.7% for the calculations of DNP enhancement. [b] The first value refers to i = 2, the second to i = 1 in $T_{i,L}$.

enhancement profile (on the left in Fig. 5), which illustrates the effect of T_2 on the saturation. (The axis are inverted since one is magnetic field and the other is frequency.)

In spite of the overall agreement, theory and experiment differ in two aspects. The first relates to the slight horizontal shift of the central hyperfine line. The second concerns the difference in the observed enhancements at the dips between the lines. Presently we cannot provide an explanation for either of these discrepancies. However, as will become apparent below, there is an indication that the performance of our current experimental setup (*e.g.*, the microwave power) might vary slightly with frequency in a nonlinear fashion.

2 Decomposing the saturation factor. A line dependent T_2 can be calculated from the diagonal entries of the matrices $\mathbb{R}_2$ or $\mathbb{T}_2$ [*cf.* eqn (B1)] as

$$T_2^{(m)} = 1/[\mathbb{R}_2]_{m,m} \text{ or } T_2^{(m)} = [\mathbb{T}_2]_{m,m}. \quad (39)$$

In the absence of Heisenberg spin exchange these two alternatives yield essentially the same numerical values. Employing this procedure, and calculating T_1 as before, we obtain (in ns)

$$T_1 = 850,\ T_2^{(1)} = 20.9,\ T_2^{(0)} = 17.8, T_2^{(-1)} = 15.4 \quad (40)$$

for the calculation corresponding to room temperature. As discussed in ref. 35, we observe that T_1 at this field essentially does not depend on the hyperfine line. This is why it is sufficient to report a single number. At the increased DNP temperature ($T \approx 40$ °C) the relaxation times are calculated as

$$T_1 = 690,\ T_2^{(1)} = 28.6,\ T_2^{(0)} = 25.1,\ T_2^{(-1)} = 22.1. \quad (41)$$

Thus, as expected, T_1 decreases and the T_2s increase with increase in temperature.

As a first approximation, let us assume that the three hyperfine lines are uncoupled. Their separate contribution to the total saturation can be calculated from

$$s = (M_z^{eq} - M_z^{ss})/M_z^{eq} = \omega_1^2 T_1 T_2/(1 + \Omega_0^2 T_2^2 + \omega_1^2 T_1 T_2), \quad (42)$$

which follows from the Bloch eqn (B5). The line-dependent steady-state saturation calculated from this equation for the T_1 and T_2 values in (41) and a microwave field B_1 = 0.9 G is shown in Fig. 6(a). The three thin lines give the contribution of the separate hyperfine lines to the total (observed) saturation, shown with a thick line. On resonance the saturation is somewhat less than 0.3 for each of the hyperfine lines. Off resonance ($\Omega_0 \neq 0$) the value of s drops due to the middle term in the denominator of eqn (42). In our case, with $\Omega_0 = \omega_A \approx 15$ G (for ^{14}N), this term is about 10 times larger than the last term. Therefore, it is reasonable to expect that only the line which is irradiated is saturated and contributes to the DNP

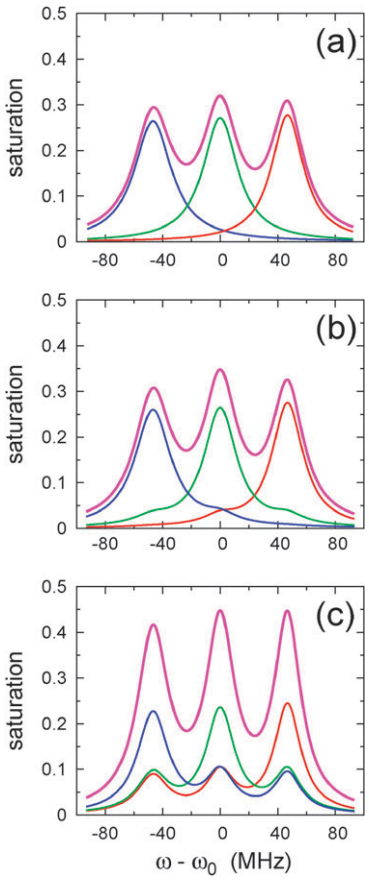

Fig. 6 Contribution of the separate hyperfine lines to the saturation at 260 GHz. (a) Independent hyperfine lines described by the classical Bloch equations. (b) Including nuclear relaxation which couples the hyperfine lines. (No Heisenberg spin exchange.) (c) Saturation under DNP conditions calculated using the parameters in Table 5.

enhancement. Thus, maximum saturation of 1/3 (for ^{14}N) or 1/2 (for ^{15}N) is generally considered. Indeed, the tails of the off-resonance lines are seen to contribute less than 10% to the total saturation [Fig. 6(a)].

To properly treat the cross-coupling of the hyperfine lines one needs to consider the matrix nature of the relaxation "times" $\mathbb{T}_1$ and $\mathbb{T}_2$ [*cf.* eqn (B1)] and solve eqn (29). The saturation calculated in this way for the parameters corresponding to the DNP conditions but without any Heisenberg spin exchange ($\tau_H = \infty$) is shown in Fig. 6(b). Cross-coupling of the hyperfine lines is evident even in the absence of Heisenberg spin exchange. Although the coupling is still relatively small, it is appreciably larger than what is obtained on the basis of the simple Bloch treatment. Note that in spite of the contribution of the neighboring off-resonance lines, the maximum total saturation does not increase dramatically compared to what was calculated for independent hyperfine lines [Fig. 6(a)] since the contribution of the on-resonance line decreases.

Lastly, we introduce Heisenberg spin exchange with $\tau_H = 400$ ns. The total saturation in this case, shown in Fig. 6(c), is exactly the one that was used to calculate the DNP enhancements in Fig. 5. The contribution of each hyperfine line to the total saturation is visible from the figure. Now that the coupling of the hyperfine lines has increased even further due to the Heisenberg spin exchange, almost half of the maximal saturation ($s \approx 0.45$) comes from the lines which are not on resonance. On resonance, saturation substantially larger than the naive expectation of 1/3 is thus obtained.

3 Sensitivity to τ_H and B_1. In this section we examine the degree to which the calculated saturation depends on the Heisenberg spin exchange rate and microwave power. To this end, we first calculate the saturation profile for twice as fast ($\tau_H = 200$ ns) and twice as slow ($\tau_H = 800$ ns) exchange rate compared to what was used in Fig. 6(c). The former value is closer to the estimate of 220 ns based on the measurement for TEMPONE in benzene.[34] As expected, faster spin exchange leads to larger saturation [Fig. 7(a)] and slower exchange to smaller saturation [Fig. 7(b)]. However, the major increase/decrease is seen to be at the peaks, with relatively little change between the hyperfine lines. This demonstrates the importance of matching the whole DNP enhancement profile as a function of microwave frequency with a given exchange rate.

The other parameter in the calculations is the amplitude of the microwave field experienced by the sample. In Fig. 8 the saturation profile is shown for a larger ($B_1 = 1.0$ G) and a smaller ($B_1 = 0.8$ G) values of the microwave field. In this case, the increase/decrease of the saturation is similar over the whole frequency range. At the same time, the lines are visibly broader for the larger B_1 and narrower for the smaller. Therefore, when calculating the profile of DNP enhancement *vs.* frequency, *e.g.*, Fig. 5, it would be hard to compensate for inaccurate estimates of B_1 by simply scaling the ε axis (that is, assuming slightly different coupling or leakage factors).

In either case, the total saturation is changed by at most 10% with respect to what was used in Fig. 5, in spite of clear differences in the relative contributions of the three hyperfine lines. This uncertainty is expected to be comparable with the

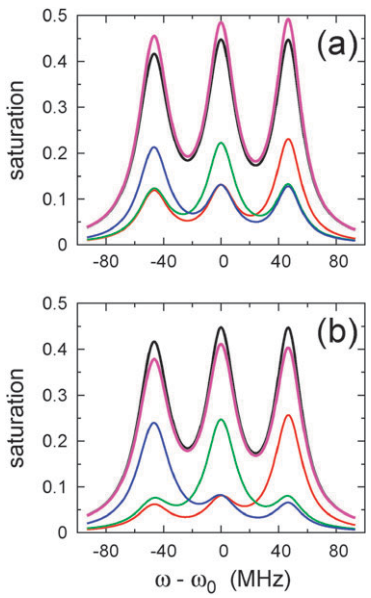

Fig. 7 Sensitivity of the saturation to the rate of Heisenberg spin exchange. (a) $\tau_H = 200$ ns. (b) $\tau_H = 800$ ns. The black line, shown as a reference, is the saturation for $\tau_H = 400$ ns. The other parameters are given in Table 5.

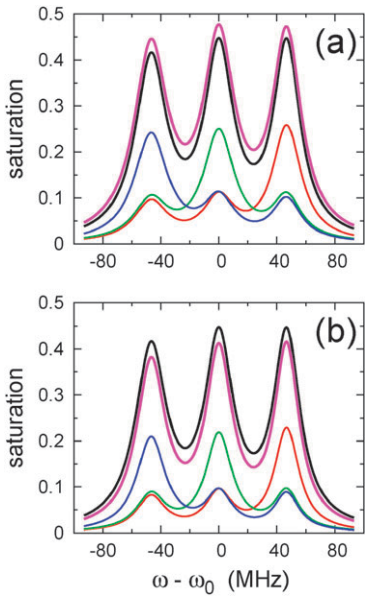

Fig. 8 Sensitivity of the saturation to the amplitude of the microwave field. (a) B_1 = 1.0 G. (b) B_1 = 0.8 G. The black line, shown as a reference, is the saturation for B_1 = 0.9 G. The other parameters are given in Table 5.

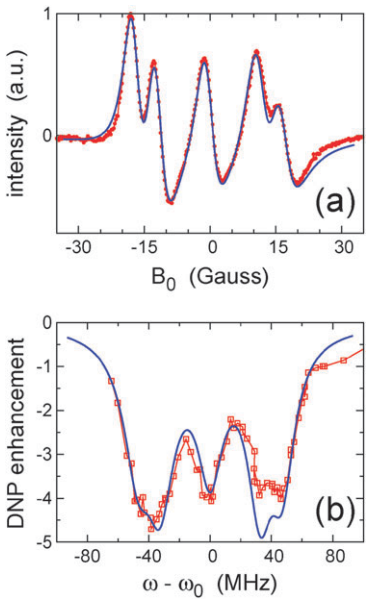

Fig. 9 Comparison of the calculated and measured cw-ESR spectra (a) and DNP enhancements (b), for the mixture of ^{14}N and ^{15}N TEMPOL in water, using the first set of simulation parameters from Table 6.

errors stemming from the calculated coupling factors and the measured DNP enhancements. Therefore, we conclude that the determined coupling factors and saturation profile are in very good agreement with the measured DNP enhancements, even after allowing τ_H and B_1 to vary in the broad range examined here.

D Uniqueness of interpretation

In the following we address the question of uniqueness. Although the enhancement profile as a function of ω_1 encodes information about various parameters (*e.g.*, ξ, f, τ_H, B_1, *etc.*) it should be explicitly stated that more than one combinations of the parameters can lead to practically the same enhancement curve. To demonstrate this point we consider a complex experimental situation and examine the cw-ESR spectra and the DNP enhancements for a mixture of 3.15 mM ^{14}N and 3.15 mM ^{15}N TEMPOL solution. The experimental and calculated cw-ESR spectra and DNP enhancement profiles are shown in Fig. 9 and 10. Two different sets of parameters were used to obtain the theoretical curves (Table 6).

From the five hyperfine lines seen in the cw spectrum, the central and the two outermost lines correspond to ^{14}N and the other two to ^{15}N. The ^{14}N : ^{15}N ratio which led to best agreement with experiment (shown in the Figures) was established to be 57 : 43 for either set of parameters. Variation in the concentrations of as little as 2% changes the relative intensities of the lines in a way which is not consistent with what is actually observed. The simulated cw spectra were obtained by adding absorption and dispersion components in a ratio of 1 to 0.5.

In the present case the cw spectra and the DNP enhancements were obtained under the same conditions (*i.e.*, maximum microwave power). Therefore, it is expected that B_1 and τ_D should be the same as the ones used in Fig. 5 (and given in

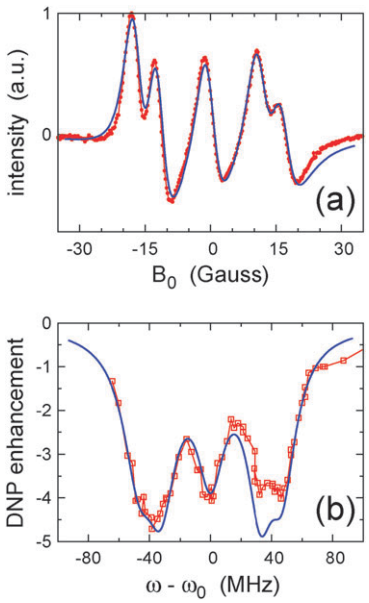

Fig. 10 Same as Fig. 9 but with the second set of parameters in Table 6.

Table 5). Furthermore, the radical concentration of 6.3 mM for the mixture implies a leakage factor of 0.731 [from (34)] and a Heisenberg spin exchange time scale of 200 ns (to be consistent with τ_H = 400 ns used for half of this concentration in Fig. 5).

However, using B_1 = 0.9 G and c = 6.3 mM (*i.e.*, f = 0.731 and τ_H = 200 ns) resulted in larger DNP enhancements than experimentally measured (not shown). This may suggest that the actual B_1 or the concentration (or both) are somewhat lower than expected. These two possibilities were separately considered. Fixing the concentration at 6.3 mM necessitated a

Table 6 Parameters for the mix of ^{14}N and ^{15}N. The ratio of 57 : 43 was deduced from the simulation of the cw spectra[a]

	τ_D/ps	B_1/G	c/mM	f	τ_H/ns	ξ (%)
cw-ESR	12	0.82	6.3	—	200	—
DNP	12	0.82	6.3	0.731	200	2.45[b]
cw-ESR	12	0.9	4.2[c]	—	300	—
DNP	12	0.9	4.2[c]	0.645	300	2.7

[a] B_0 = 92123.8 G for all simulations. The dispersive component is 0.5 for the cw simulations. [b] The reduced microwave power implies lower temperature by about 5 °C, which leads to smaller ξ. [c] The concentration is deduced from the value of the leakage factor and is used to calculate τ_H.

lower B_1 of 0.82 G for the agreement with experiment shown in Fig. 9. Since the lower microwave power (compared to what was used in Fig. 5) implies a decrease in the sample temperature by about 5 °C, the coupling factor was decreased to a value appropriate for T = 35 °C (ξ = 2.45%). Alternatively, keeping B_1 at the expected value of 0.9 G, agreement between theory and experiment was obtained for c = 4.2 mM (that is f = 0.645 and τ_H = 300 ns) as shown in Fig. 10.

The comparison of Fig. 9 and 10 reveals that the two sets of parameters given in Table 6 both lead to reasonably good agreement with the experimental data. It should be apparent, therefore, that the experimental information does not correspond to a unique combination of the parameters. A certain degree of compensation is evidently possible by changing the experimental variables in a concerted fashion.

The determined ratio of 57 : 43 for the ^{14}N–^{15}N mixture at hand demonstrates that uncertainties in the concentration of up to 15% can be expected for the samples employed in the current study. This number is smaller than the 30% difference that had to be assumed in the simulations of Fig. 10. Therefore, the calculation with the reduced concentration likely does not correspond to the experimental situation. Our purpose in presenting it, however, is to demonstrate the room for compensation that is possible when different parameters are changed simultaneously.

In contrast, the deviation of the microwave power from what is expected on the basis of Fig. 5 is well justified from an experimental point of view. The power in the cavity may drop depending on experimental conditions which are hard to reproduce exactly. In fact, variations of the microwave field of such magnitude are not only expected but are present across the frequency range swept in a single experiment, as demonstrated by the discrepancy between theory and experiment at the higher frequency part of the enhancement curves in both Fig. 9(b) and 10(b). With either set of simulation parameters the calculations predict that the DNP enhancements should be somewhat larger at the positive microwave frequencies compared to the negative frequencies (with the central hyperfine line at the origin). The observed enhancements show the opposite trend, which is hard to rationalize in the context of the cw-ESR spectra. Hence, we suspect that this discrepancy is caused by the slightly worse performance of the experimental setup at the frequencies corresponding to the hyperfine lines on the right hand side of Fig. 9(b) and 10(b).

V. Concluding remarks

In this study DNP enhancements at 9.2 T were calculated as a function of microwave frequency for the nitroxide radical TEMPOL in water. The calculated enhancements showed very good agreement with the experimental results for the same system. Two complementary pieces of information were necessary for the direct comparison with experiment: the coupling factor and the saturation factor. The DNP coupling factor for TEMPOL and water at 260 GHz/400 MHz was calculated from MD simulations in paper I. In the present article we treated the saturation of the electronic spin by carefully accounting for the various mechanisms of spin relaxation within the rigorous framework of semiclassical (Redfield) relaxation theory.

Being an approximate, second order perturbative treatment the theory has a limited range of applicability, which breaks when the dynamics of the spin bearing molecule is sufficiently slow. Due to their relatively small size, the nitroxide radicals typically used as polarizing agents in liquid-state DNP experiments tumble fast enough in solution to justify this approximate treatment. Care has to be exercised when extending the present approach to larger radicals or spin labeled proteins.

Two main conclusions can be drawn from the present study. The first relates to the treatment of the electron spin saturation in the interpretation of DNP enhancement experiments with nitroxides. We have shown that the saturation behavior of the three hyperfine lines cannot be described properly assuming that the lines are independent and using the classical Bloch equations. Remarks along those lines are common in the literature (*e.g.*, ref. 1) but few studies have actually attempted to systematically address the issue.[4,36] In ref. 4 and 36 the cross-coupling of the three hyperfine lines due to nitrogen nuclear spin relaxation[4] and Heisenberg spin exhange[4,36] was modeled by considering the 12 populations of the three-spin system electron–nitrogen–proton. In contrast, in our treatment of the saturation, we have neglected the electron spin relaxation due to its dipolar coupling to the proton nuclear spin, thus working only with the two-spin system electron–nitrogen. However, unlike the model of ref. 4 and 36, the electron spin coherences are explicitly present in our analysis. Accounting for the dynamics of the coherences is important for the description of T_2 processes, which clearly affect the degree of saturation already at the level of the classical Bloch equations [*cf.* eqn (42)]. In the case of the "generalized Bloch equations" that we have derived [eqn (26)] the coupling of the three hyperfine lines is captured by the matrix nature of the relaxation times $\mathbb{T}_1$ and $\mathbb{T}_2$ [eqn (B1)]. It is evident that such coupling (*e.g.*, due to Hesienberg spin exchange) happens not only through $\mathbb{T}_1$ processes, but also through $\mathbb{T}_2$ processes [*cf.* eqn (B1)]. The agreement between the DNP enhancement profiles calculated using our formalism and experiment suggests that the dipolar coupling of the electron spin with the proton nuclear spins can indeed be ignored in the calculation of the saturation factor. Needless to say, this coupling is essential for the DNP phenomenon, and its effect was taken into account in the calculation of the coupling factor.

The second conclusion concerns the use of MD simulations to calculate *electronic* T_1 and T_2 relaxation rates from first

principles. Our results demonstrate that MD simulations reflect the dynamics of TEMPOL in water surprisingly well. This applies not only to the overall tumbling, which occurs on a time scale of about 20 ps and has a strong influence on the T_2 at 260 GHz, but also to the inertial part of the rotational motion, which occurs on a time scale of about 0.1 ps and influences the value of T_1 through spin-rotation coupling. From that perspective, the calculation of electronic spin relaxation emerges as a means for very serious validation of the *dynamics* aspect of MD simulations. Even longer time scales, in the range from hundreds of picoseconds to tens of nanoseconds, become important in the context of spin labels attached to proteins. There is already evidence that MD simulations do surprisingly well in this regime as well.[33]

Appendix A: Relaxation operators

1 Tumbling and spin-rotation coupling

Using the form of the Hamiltonian given in the text and the fact that all the spectral densities are even functions of ω one obtains the following expressions for the relaxation operators under the assumption of isotropic tumbling:

$$R_{LL}(\cdot) = J^{\eta+\zeta}(0)[\hat{S}_z,[\hat{S}_z,\cdot]] + \frac{1}{2}J^{\eta+\zeta}(\omega)([\hat{S}_-,[\hat{S}_+,\cdot]]+[\hat{S}_+,[\hat{S}_-,\cdot]]), \tag{A1a}$$

$$R_{ZZ}(\cdot) = \frac{2}{3}J^{GG}(0)[\hat{S}_z,[\hat{S}_z,\cdot]] + \frac{1}{4}J^{GG}(\omega)([\hat{S}_-,[\hat{S}_+,\cdot]]+[\hat{S}_+,[\hat{S}_-,\cdot]]), \tag{A1b}$$

$$R_{ZN}(\cdot) = \frac{2}{3}J^{GA}(0)([\hat{S}_z,[\hat{I}_z\hat{S}_z,\cdot]]+[\hat{I}_z\hat{S}_z,[\hat{S}_z,\cdot]]) + \frac{1}{4}J^{GA}(\omega)([\hat{S}_-,[\hat{I}_z\hat{S}_+,\cdot]]+[\hat{I}_z\hat{S}_-,[\hat{S}_+,\cdot]] + [\hat{S}_+,[\hat{I}_z\hat{S}_-,\cdot]]+[\hat{I}_z\hat{S}_+,[\hat{S}_-,\cdot]]), \tag{A1c}$$

$$R_{NN}(\cdot) = J^{AA}(0)\left(\frac{2}{3}[\hat{I}_z\hat{S}_z,[\hat{I}_z\hat{S}_z,\cdot]]+\frac{1}{4}[\hat{I}_+\hat{S}_z,[\hat{I}_-\hat{S}_z,\cdot]] + \frac{1}{4}[\hat{I}_-\hat{S}_z,[\hat{I}_+\hat{S}_z,\cdot]]\right) + \frac{1}{4}J^{AA}(\omega)([\hat{I}_z\hat{S}_-,[\hat{I}_z\hat{S}_+,\cdot]]+[\hat{I}_z\hat{S}_+,[\hat{I}_z\hat{S}_-,\cdot]] + \frac{1}{6}[\hat{I}_+\hat{S}_-,[\hat{I}_-\hat{S}_+,\cdot]]+\frac{1}{6}[\hat{I}_-\hat{S}_+,[\hat{I}_+\hat{S}_-,\cdot]] + [\hat{I}_+\hat{S}_+,[\hat{I}_-\hat{S}_-,\cdot]]+[\hat{I}_-\hat{S}_-,[\hat{I}_+\hat{S}_+,\cdot]]). \tag{A1d}$$

Here,

$$J^{XY}(\omega) = c^{XY}\tau_D/(1+\omega^2\tau_D^2) \tag{A2}$$

are the rotational spectral densities (assuming the rotational correlation function is exponentially decaying), $\tau_D = 1/6D$ is the rotational correlation time corresponding to a diffusion coefficient D, and the coefficients[21]

$$c^{GG} = \gamma_e^2 B_0^2\,\mathrm{Tr}\{\mathsf{G}'\mathsf{G}'\}/5,\quad c^{GA} = \gamma_e^2 B_0\,\mathrm{Tr}\{\mathsf{G}'\mathsf{A}'\}/5,\quad c^{AA} = \gamma_e^2\mathrm{Tr}\{\mathsf{A}'\mathsf{A}'\}/5 \tag{A3}$$

are defined in terms of the traceless magnetic tensors.

The spectral density

$$J^{\eta+\zeta}(\omega) = J^{\eta}(\omega) + J^{\zeta}(\omega) \tag{A4}$$

appears in the contribution of the spin-rotation coupling, where $J^{\eta}(\omega)$ and $J^{\zeta}(\omega)$ are associated with $\hat{L}_1$ and $\hat{L}_2$, respectively [*cf.* eqn (13)]. They are related to the auto-correlation functions $C^{\eta}(\tau)$ and $C^{\zeta}(\tau)$ of the angular velocity $\boldsymbol{\eta}$ and the vector $\boldsymbol{\zeta}$ through

$$J(\omega) = \mathrm{Re}\int_0^{\infty}\mathrm{d}\tau e^{-i\omega\tau}C(\tau). \tag{A5}$$

Cross-correlations between $\boldsymbol{\eta}$ and $\boldsymbol{\zeta}$ vanish if one assumes that the orientation of the molecule is independent of its angular momentum.[22] For an exponentially decaying C^{η}, *i.e.*, $C^{\eta}(\tau) = T_0^2 c^{\eta} e^{-\tau/\tau_{\eta}}$, one has

$$J^{\eta}(\omega) = T_0^2 c^{\eta}\tau_{\eta}/(1+\omega^2\tau_{\eta}^2). \tag{A6}$$

The contribution of $\hat{L}_2$ requires the evaluation of similar correlation functions but after replacing $\boldsymbol{\eta}$ by $\boldsymbol{\zeta}$. When the angular velocity decorrelates much faster than the coupling tensor T ($\tau_{\eta} \ll \tau_D$), which is the case in liquids, the correlation functions of $\boldsymbol{\zeta}$ can be factorized to a good approximation.[22] In the case of exponential decay, this leads to $C^{\zeta}(\tau) \approx T'^2 c^{\eta} e^{-\tau/\tau_{\eta}}$, with $T'^2 = \mathrm{Tr}\{\mathsf{T}'\mathsf{T}'\}/3$.[37] The corresponding spectral density J^{ζ} is like the one shown in eqn (A6) but with T_0^2 replaced by T'^2. Therefore, for their sum we obtain

$$J^{\eta+\zeta}(\omega) = (T_0^2 + T'^2)[c^{\eta}\tau_{\eta}/(1+\omega^2\tau_{\eta}^2)]. \tag{A7}$$

If the decay of the correlation function is non-exponential the part in square brackets needs to be modified accordingly [*cf.* eqn (37)].

Substituting the density matrix from eqn (19) and simplifying due to $S = 1/2$ leads to

$$R_{LL}(\rho_{\pm}\hat{S}_{\mp}) = [J^{\eta+\zeta}(0) + J^{\eta+\zeta}(\omega)]\rho_{\pm}\hat{S}_{\mp},\quad R_{LL}(\rho_z 2\hat{S}_z) = 2J^{\eta+\zeta}(\omega)\rho_z 2\hat{S}_z,\quad R_{LL}(\rho_0\hat{S}_0) = 0, \tag{A8}$$

$$R_{ZZ}(\rho_{\pm}\hat{S}_{\mp}) = [\tfrac{2}{3}J^{GG}(0) + \tfrac{1}{2}J^{GG}(\omega)]\rho_{\pm}\hat{S}_{\mp},\quad R_{ZZ}(\rho_z 2\hat{S}_z) = J^{GG}(\omega)\rho_z 2\hat{S}_z,\quad R_{ZZ}(\rho_0\hat{S}_0) = 0, \tag{A9}$$

$$R_{ZN}(\rho_{\pm}\hat{S}_{\mp}) = [\tfrac{2}{3}J^{GA}(0) + \tfrac{1}{2}J^{GA}(\omega)]\{\hat{I}_z,\rho_{\pm}\}\hat{S}_{\mp},\quad R_{ZN}(\rho_z 2\hat{S}_z) = J^{GA}(\omega)\{\hat{I}_z,\rho_z\}2\hat{S}_z,\quad R_{ZN}(\rho_0\hat{S}_0) = 0, \tag{A10}$$

$$R_{NN}(\rho_{\pm}\hat{S}_{\mp}) = \frac{1}{4}J^{AA}(0)\left(\frac{2}{3}\{\hat{I}_z,\{\hat{I}_z,\rho_{\pm}\}\}\right.$$
$$\left.+\frac{1}{4}\{\hat{I}_+,\{\hat{I}_-,\rho_{\pm}\}\}+\frac{1}{4}\{\hat{I}_-,\{\hat{I}_+,\rho_{\pm}\}\}\right)\hat{S}_{\mp}$$
$$+\frac{1}{4}J^{AA}(\omega)\left\{\left(\frac{1}{6}\hat{I}_{\pm}\hat{I}_{\mp}+\hat{I}_z\hat{I}_z+\hat{I}_{\mp}\hat{I}_{\pm}\right)\rho_{\pm}\right.$$
$$\left.+\rho_{\pm}\left(\frac{1}{6}\hat{I}_{\mp}\hat{I}_{\pm}+\hat{I}_z\hat{I}_z+\hat{I}_{\pm}\hat{I}_{\mp}\right)\right\}\hat{S}_{\mp} \quad \text{(A11a)}$$

$$R_{NN}(\rho_z 2\hat{S}_z) = \frac{1}{4}J^{AA}(0)\left(\frac{2}{3}[\hat{I}_z,[\hat{I}_z,\rho_z]]\right.$$
$$\left.+\frac{1}{4}[\hat{I}_+,[\hat{I}_-,\rho_z]]+\frac{1}{4}[\hat{I}_-,[\hat{I}_+,\rho_z]]\right)2\hat{S}_z$$
$$+\frac{1}{4}J^{AA}(\omega)\left(\frac{7}{12}\{\hat{I}_+,\{\hat{I}_-,\rho_z\}\}+\frac{7}{12}\{\hat{I}_-,\{\hat{I}_+,\rho_z\}\}\right.$$
$$\left.+\{\hat{I}_z,\{\hat{I}_z,\rho_z\}\}\right)2\hat{S}_z$$
$$+\frac{5}{48}J^{AA}(\omega)([\hat{I}_+,\{\hat{I}_-,\rho_z\}]-[\hat{I}_-,\{\hat{I}_+,\rho_z\}])\hat{S}_0, \quad \text{(A11b)}$$

$$R_{NN}(\rho_0\hat{S}_0) = \frac{1}{4}J^{AA}(0)\left(\frac{2}{3}[\hat{I}_z,[\hat{I}_z,\rho_0]]\right.$$
$$\left.+\frac{1}{4}[\hat{I}_+,[\hat{I}_-,\rho_0]]+\frac{1}{4}[\hat{I}_-,[\hat{I}_+,\rho_0]]\right)\hat{S}_0$$
$$+\frac{1}{4}J^{AA}(\omega)\left(\frac{7}{12}[\hat{I}_+,[\hat{I}_-,\rho_0]]+\frac{7}{12}[\hat{I}_-,[\hat{I}_+,\rho_0]]\right.$$
$$\left.+[\hat{I}_z,[\hat{I}_z,\rho_0]]\right)\hat{S}_0$$
$$+\frac{5}{48}J^{AA}(\omega)(\{\hat{I}_+,[\hat{I}_-,\rho_0]\}-\{\hat{I}_-,[\hat{I}_+,\rho_0]\})2\hat{S}_z \quad \text{(A11c)}$$

for the relaxation, and

$$[\hat{H}'_0,\rho_{\pm}\hat{S}_{\mp}] = \mp\left(\Omega_0\rho_{\pm}+\frac{1}{2}\omega_A\{\hat{I}_z,\rho_{\pm}\}\right)\hat{S}_{\mp}\pm\frac{1}{2}\omega_1\rho_{\pm}2\hat{S}_z,$$
$$[\hat{H}'_0,\rho_z 2\hat{S}_z] = \frac{1}{2}\omega_A[\hat{I}_z,\rho_z]\hat{S}_0-\omega_1\rho_z(\hat{S}_+-\hat{S}_-),$$
$$[\hat{H}'_0,\rho_0\hat{S}_0] = \omega_A[\hat{I}_z,\rho_0]\hat{S}_z \quad \text{(A12)}$$

for the coherent evolution. In these equations $\{\cdot,\cdot\}$ denotes anticommutator. None of these expressions couple the diagonal elements of ρ_κ to the off-diagonal elements. Their action on the diagonal elements depends on whether we deal with a nitrogen spin $I = 1$ or $I = 1/2$. These two cases are treated separately next.

a $I = 1$. In this case one finds from eqn (A8) to (A11) that

$$\mathbb{R}_2 = a_2\mathbb{I}_0+b_2\mathbb{I}_z+c_2\mathbb{I}_z^2+d_2(\mathbb{I}_++\mathbb{I}_-)/\sqrt{2},$$
$$\mathbb{R}_1 = a_1\mathbb{I}_0+b_1\mathbb{I}_z+c_1\mathbb{I}_z^2+d_1(\mathbb{I}_++\mathbb{I}_-)/\sqrt{2}, \quad \text{(A13)}$$

where

$$a_2 = c^{GG}[4J(0)+3J(\omega)]/6+[J^{\eta+\xi}(0)+J^{\eta+\xi}(\omega)]$$
$$+c^{AA}[3J(0)+7J(\omega)]/6$$
$$b_2 = c^{GA}[4J(0)+3J(\omega)]/3,$$
$$c_2 = c^{AA}[5J(0)-J(\omega)]/12,\ d_2 = c^{AA}J(0)/4, \quad \text{(A14)}$$

and

$$a_1 = c^{GG}J(\omega)+2J^{\eta+\xi}(\omega)+c^{AA}[3J(0)+7J(\omega)]/6,$$
$$b_1 = c^{GA}2J(\omega),\ c_1 = c^{AA}[5J(\omega)-3J(0)]/12,$$
$$d_1 = c^{AA}[7J(\omega)-3J(0)]/12. \quad \text{(A15)}$$

Before writing down the expressions for $\mathbb{R}_0$, $\mathbb{U}$, and $\mathbb{V}$ we point to the presence of the identity matrix $\hat{I}_0\hat{S}_0$ in the sub-matrix ρ_0. Since this part of the density matrix does not evolve it leads to a singular matrix-inversion problem.[9] This difficulty is easily removed by changing the basis for the main diagonal of ρ_0 by introducing

$$(\rho_0)_{\text{diag}} = \sigma_{00}\hat{I}_0+\sigma_{01}\hat{I}_z+\sigma_{02}\hat{I}_z^2, \quad \text{(A16)}$$

and subsequently discarding the scalar σ_{00}. This leaves only two entries for the vector σ_0, defined in eqn (21), namely σ_{01} and σ_{02}. As a result, $\mathbb{R}_0$ becomes a 2×2 matrix, whereas $\mathbb{U}$, and $\mathbb{V}$ become 3×2 and 2×3 matrices, respectively. For their matrix representations we find

$$\mathbb{R}_0 = e\begin{bmatrix}1 & 0\\ 0 & 3\end{bmatrix},\ \mathbb{U} = f\frac{1}{2}\begin{bmatrix}1 & 3\\ 2 & 0\\ 1 & -3\end{bmatrix},\ \mathbb{V} = f\begin{bmatrix}1 & 2 & 1\\ 1 & 0 & -1\end{bmatrix}, \quad \text{(A17)}$$

where

$$e = c^{AA}[3J(0)+7J(\omega)]/12,\ f = c^{AA}5J(\omega)/12. \quad \text{(A17)}$$

b $I = 1/2$. Proceeding as before we obtain

$$\mathbb{R}_2 = a_2\mathbb{I}_0+b_2\mathbb{I}_z+d_2(\mathbb{I}_++\mathbb{I}_-),$$
$$\mathbb{R}_1 = a_1\mathbb{I}_0+b_1\mathbb{I}_z+d_1(\mathbb{I}_++\mathbb{I}_-), \quad \text{(A19)}$$

where

$$a_2 = c^{GG}[4J(0)+3J(\omega)]/6+[J^{\eta+\xi}(0)+J^{\eta+\xi}(\omega)]$$
$$+c^{AA}[7J(0)+10J(\omega)]/24 \quad \text{(A20)}$$
$$b_2 = c^{GA}[4J(0)+3J(\omega)]/3,\ d_2 = c^{AA}J(0)/8,$$

and

$$a_1 = c^{GG}J(\omega)+2J^{\eta+\xi}(\omega)+c^{AA}[3J(0)+14J(\omega)]/24,$$
$$b_1 = c^{GA}J(\omega),\ d_1 = c^{AA}[7J(\omega)-3J(0)]/24. \quad \text{(A21)}$$

Again, to isolate the trace of the density matrix we write

$$(\rho_0)_{\mathrm{diag}} = \sigma_{00}\hat{I}_0 + \sigma_{01}2\hat{I}_z \tag{A22}$$

and discard the scalar σ_{00}. This leads to

$$\mathbb{R}_0 = e,\ \mathbb{U} = f\begin{bmatrix}1\\1\end{bmatrix},\ \mathbb{V} = 2f[\,1 \quad 1\,], \tag{A23}$$

with

$$e = c^{AA}[3J(0) + 7J(\omega)]/12,\ f = c^{AA}5J(\omega)/24. \tag{A24}$$

2 Heisenberg spin exchange

a Pure $I = 1$ or $I = 1/2$. In addition to the relaxation due to tumbling and spin-rotation coupling we include relaxation caused by Heisenberg spin exchange between two nitroxides. We follow ref. 38 in the construction of the exchange relaxation operator X. In general, X is nonlinear but it can be linearized assuming the high-temperature approximation holds.[38] Using Greek indices to denote the state of the (nonexchanging) nuclear spin and Latin indices for the state of the (exchanging) electronic spin, for the matrix elements of $X(\rho)$ one has[8,38]

$$\langle i\alpha|X(\rho)|j\beta\rangle = \tau_{\mathrm{H}}^{-1}\Big[\langle i\alpha|\rho|j\beta\rangle - \frac{1}{2}\delta_{ij}\sum_k\langle k\alpha|\rho|k\beta\rangle - N_n^{-1}\delta_{\alpha\beta}\sum_\gamma\langle i\gamma|\rho|j\gamma\rangle\Big], \tag{A25}$$

where N_n is the dimension of the nuclear spin Hilbert space (equal to 3 or 2). From this expression one obtains

$$\mathbb{X} = \frac{1}{3}\begin{bmatrix}2 & -1 & -1\\ -1 & 2 & -1\\ -1 & -1 & 2\end{bmatrix} \tag{A26}$$

in the case of $I = 1$, and

$$\mathbb{X} = \frac{1}{2}\begin{bmatrix}1 & -1\\ -1 & 1\end{bmatrix} \tag{A27}$$

in the case of $I = 1/2$.

b Mixture of $I = 1$ and $I = 1/2$. The Heisenberg exchange between ^{14}N (with density matrix ρ_3) and ^{15}N (with ρ_2) is given by[38]

$$\langle i\alpha|X(\rho_3)|j\beta\rangle = \tau_{\mathrm{H}}^{-1}\Big[\langle i\alpha|\rho_3|j\beta\rangle - \frac{1}{2}\delta_{ij}\sum_k\langle k\alpha|\rho_3|k\beta\rangle - N_2^{-1}\delta_{\alpha\beta}\sum_\gamma\langle i\gamma|\rho_2|j\gamma\rangle\Big] \tag{A28}$$

and

$$\langle i\alpha|X(\rho_2)|j\beta\rangle = \tau_{\mathrm{H}}^{-1}\Big[\langle i\alpha|\rho_2|j\beta\rangle - \frac{1}{2}\delta_{ij}\sum_k\langle k\alpha|\rho_2|k\beta\rangle - N_3^{-1}\delta_{\alpha\beta}\sum_\gamma\langle i\gamma|\rho_3|j\gamma\rangle\Big], \tag{A29}$$

assuming the rate of exchange, τ_{H}^{-1}, is the same for the two isotopes. Using these expressions together with $N_3 = 3$ and $N_2 = 2$ we find

$$X(\sigma_3)_k^{(m)} = \tau_{\mathrm{H}}^{-1}[\sigma_{3,k}^{(m)} - \tfrac{1}{2}(\sigma_{2,k}^{(+)} + \sigma_{2,k}^{(-)})] \tag{A30}$$

and

$$X(\sigma_2)_k^{(n)} = \tau_{\mathrm{H}}^{-1}[\sigma_{2,k}^{(m)} - \tfrac{1}{3}(\sigma_{3,k}^{(1)} + \sigma_{3,k}^{(0)} + \sigma_{3,k}^{(\bar{1})})] \tag{A31}$$

for $\kappa = z, +, -$. These expressions for cross-isotope exchange should be added to the previously derived eqn (A26) and (A27) in the appropriate ratio, determined by the relative concentration of the two species.

Appendix B: Eqn (29) and the steady-state solution of the Bloch equations

In complete analogy to the Bloch equations, it is possible to write the steady-state solution (29) more explicitly. To do so we introduce the matrices

$$\mathbb{T}_2^{-1} = \mathbb{R}_2 + \mathbb{X}/\tau_{\mathrm{H}},\ \mathbb{T}_1^{-1} = \mathbb{R}_1 + \mathbb{X}/\tau_{\mathrm{H}},\ \mathbb{T}_0^{-1} = \mathbb{R}_0, \tag{B1}$$

and define the combinations

$$\begin{aligned}\mathbb{O} &= \Omega_0\mathbb{I}_0 + \omega_A\mathbb{I}_z,\\ \mathbb{P} &= \mathbb{I}_0 + \mathbb{O}\mathbb{T}_2\mathbb{O}\mathbb{T}_2,\\ \mathbb{Q} &= \mathbb{I}_0 - \mathbb{T}_1\mathbb{U}\mathbb{T}_0\mathbb{V},\end{aligned} \tag{B2}$$

where $\mathbb{O}$ has units of frequency, and $\mathbb{P}$ and $\mathbb{Q}$ are dimensionless. The steady-state solution is found to be

$$\begin{aligned}\sigma_x^{\mathrm{ss}} &= \omega_1\mathbb{T}_2\mathbb{O}\mathbb{T}_2(\mathbb{Q}\mathbb{P} + \omega_1^2\mathbb{T}_1\mathbb{T}_2)^{-1}\mathbb{Q}\sigma_z^{\mathrm{eq}},\\ \sigma_y^{\mathrm{ss}} &= -\omega_1\mathbb{T}_2(\mathbb{Q}\mathbb{P} + \omega_1^2\mathbb{T}_1\mathbb{T}_2)^{-1}\mathbb{Q}\sigma_z^{\mathrm{eq}},\\ \sigma_z^{\mathrm{ss}} &= \mathbb{P}(\mathbb{Q}\mathbb{P} + \omega_1^2\mathbb{T}_1\mathbb{T}_2)^{-1}\mathbb{Q}\sigma_z^{\mathrm{eq}},\\ \sigma_0^{\mathrm{ss}} &= \mathbb{T}_0\mathbb{V}[\mathbb{I}_0 - \mathbb{P}(\mathbb{Q}\mathbb{P} + \omega_1^2\mathbb{T}_1\mathbb{T}_2)^{-1}\mathbb{Q}]\sigma_z^{\mathrm{eq}}.\end{aligned} \tag{B3}$$

In this form, the calculation is seen to involve the single inversion of a real 3×3 or 2×2 matrix, in addition to several matrix multiplications. This might be preferred over the equivalent eqn (29) which involves the inversion of an 11×11 or 7×7 matrix. For the derivatives of σ_x^{ss} and σ_y^{ss} with respect to ω we find

$$\begin{aligned}\frac{\partial\sigma_y^{\mathrm{ss}}}{\partial\omega} &= \mathbb{T}_2(\mathbb{Q}\mathbb{P} + \omega_1\mathbb{T}_1\mathbb{T}_2)^{-1}\mathbb{Q}(\mathbb{T}_2\mathbb{O} + \mathbb{O}\mathbb{T}_2)\sigma_y^{\mathrm{ss}},\\ \frac{\partial\sigma_x^{\mathrm{ss}}}{\partial\omega} &= \mathbb{T}_2\left(\sigma_y^{\mathrm{ss}} - \mathbb{O}\frac{\partial\sigma_y^{\mathrm{ss}}}{\partial\omega}\right).\end{aligned} \tag{B4}$$

In section IV, eqn (B3) and (B4) were used to, respectively, calculate the saturation and simulate cw-ESR spectra of TEMPOL.

Naturally, in the absence of the nitrogen spin, *i.e.*, when $\mathbb{Q} = \mathbb{I}_0$, the solution (B3) reduces to the steady-state solution of the familiar Bloch equations:

$$\begin{aligned}M_x^{\mathrm{ss}} &= \omega_1\Omega_0T_2^2(1 + \Omega_0^2T_2^2 + \omega_1^2T_1T_2)^{-1}M_z^{\mathrm{eq}},\\ M_y^{\mathrm{ss}} &= -\omega_1T_2(1 + \Omega_0^2T_2^2 + \omega_1^2T_1T_2)^{-1}M_z^{\mathrm{eq}},\\ M_z^{\mathrm{ss}} &= (1 + \Omega_0^2T_2^2)(1+\Omega_0^2T_2^2 + \omega_1^2T_1T_2)^{-1}M_z^{\mathrm{eq}}.\end{aligned} \tag{B5}$$

Acknowledgements

Funding from the European Union BioDNP Project is gratefully acknowledged.

References

1 P. Höfer, G. Parigi, C. Luchinat, P. Carl, G. Guthausen, M. Reese, T. Carlomagno, C. Griesinger and M. Bennati, *J. Am. Chem. Soc.*, 2008, **130**, 3254.
2 M. J. Prandolini, V. P. Denysenkov, M. Gafurov, B. Endeward and T. F. Prisner, *J. Am. Chem. Soc.*, 2009, **131**, 6090.
3 K. H. Hausser and D. Stehlik, *Adv. Magn. Reson.*, 1968, **3**, 79.
4 B. D. Armstrong and S. Han, *J. Chem. Phys.*, 2007, **127**, 104508.
5 E. R. McCarney, B. D. Armstrong, R. Kausik and S. Han, *Langmuir*, 2008, **24**, 10062.
6 B. D. Armstrong and S. Han, *J. Am. Chem. Soc.*, 2009, **131**, 4641.
7 J. H. Freed, *J. Chem. Phys.*, 1965, **43**, 2312.
8 J. H. Freed, *J. Phys. Chem.*, 1967, **71**, 38.
9 M. P. Eastman, R. G. Kooser, M. R. Das and J. H. Freed, *J. Chem. Phys.*, 1969, **51**, 2690.
10 M. Prandolini, V. P. Denysenkov, M. Gafurov, S. Lyubenova, B. Endeward, M. Bennati and T. Prisner, *Appl. Magn. Reson.*, 2008, **34**, 399.
11 A. Abragam, *The Principles of Nuclear Magnetism*, Oxford University Press, New York, 1961.
12 M. Goldman, *J. Magn. Reson.*, 2001, **149**, 160.
13 B. L. Bales and M. Peric, *J. Phys. Chem. B*, 1997, **101**, 8707.
14 K. M. Salikhov, *J. Magn. Reson.*, 1985, **63**, 271.
15 W. Hofbauer, K. A. Earle, C. R. Dunnam, J. K. Moscicki and J. H. Freed, *Rev. Sci. Instrum.*, 2004, **75**, 1194.
16 J. S. Hyde, J.-J. Yin, W. K. Subczynski, T. G. Camenisch, J. J. Ratke and W. Froncisz, *J. Phys. Chem. B*, 2004, **108**, 9524.
17 W. Froncisz, T. G. Camenisch, J. J. Ratke, J. R. Anderson, W. K. Subczynski, R. A. Strangeway, J. W. Sidabras and J. S. Hyde, *J. Magn. Reson.*, 2008, **193**, 297.
18 D. E. Budil, K. A. Earle and J. H. Freed, *J. Phys. Chem.*, 1993, **97**, 1294.
19 C. Mailer, R. D. Nielsen and B. H. Robinson, *J. Phys. Chem. A*, 2005, **109**, 4049.
20 S. S. Eaton and G. R. Eaton, in *Biological Magnetic Resonance, Volume 19: Distance Measurements in Biological Systems by EPR*, Kluwer Academic/Plenum Publishers, New York, 2000, pp. 29–154.
21 N. M. Atherton, *Principles of Electron Spin Resonance*, Ellis Horwood PTR Prentice Hall, 1993.
22 P. S. Hubbard, *Phys. Rev.*, 1963, **131**, 1155.
23 L. Werbelow and R. E. London, *Concepts Magn. Reson.*, 1996, **8**, 325.
24 V. P. Denysenkov, M. J. Prandolini, A. Krahn, M. Gafurov, B. Endeward and T. F. Prisner, *Appl. Magn. Reson.*, 2008, **34**, 289.
25 W. L. Jorgensen, J. Chandrasekhar, J. D. Madura, R. W. Impey and M. L. Klein, *J. Chem. Phys.*, 1983, **79**, 926.
26 D. Sezer, J. H. Freed and B. Roux, *J. Phys. Chem. B*, 2008, **112**, 5755.
27 J. C. Phillips, R. Braun, W. Wang, J. Gumbart, E. Tajkorshid, E. Villa, C. Chipot, R. D. Skeel, L. Kale and K. Schulten, *J. Comput. Chem.*, 2005, **26**, 1781.
28 U. Essmann, L. Perera, M. L. Berkowitz, T. Darden, H. Lee and L. G. Pedersen, *J. Chem. Phys.*, 1995, **103**, 8577.
29 S. Miyamoto and P. A. Kollman, *J. Comput. Chem.*, 1992, **13**, 952.
30 D. Marsh, D. Kurad and V. A. Livshits, *Chem. Phys. Lipids*, 2002, **116**, 93.
31 J. P. Barnes, Z. Liang, H. S. Mchaourab, J. H. Freed and W. L. Hubbell, *Biophys. J.*, 1999, **76**, 3298.
32 Z. Liang, Y. Lou, J. H. Freed, L. Columbus and W. L. Hubbell, *J. Phys. Chem. B*, 2004, **108**, 17649.
33 D. Sezer, J. H. Freed and B. Roux, *J. Am. Chem. Soc.*, 2009, **131**, 2597.
34 I. V. Koptyug, S. H. Bossmann and N. J. Turro, *J. Am. Chem. Soc.*, 1996, **118**, 1435.
35 B. H. Robinson, A. W. Reese, E. Gibbons and C. Mailer, *J. Phys. Chem. B*, 1999, **103**, 5881.
36 R. D. Bates and W. S. Drozdoski, *J. Chem. Phys.*, 1977, **67**, 4038.
37 G. Nyberg, *Mol. Phys.*, 1967, **12**, 69.
38 S. Alexander, *J. Chem. Phys.*, 1962, **37**, 974.